Inhibition of miR-25 ameliorates cardiac and skeletal muscle dysfunction in aged *mdx/utrn* haploinsufficient (+/−) mice

Sacha V. Kepreotis,[2,5] Jae Gyun Oh,[2,5] Mina Park,[1,5] Jimeen Yoo,[2] Cholong Lee,[1] Mark Mercola,[3] Roger J. Hajjar,[4] and Dongtak Jeong[1,2]

[1]Department of Medicinal and Life Science, College of Science and Convergence Technology, Hanyang University-ERICA, Ansan, South Korea; [2]Cardiovascular Research Institute, Icahn School of Medicine, Mount Sinai, NY, USA; [3]Stanford Cardiovascular Institute, Stanford University School of Medicine, Stanford, CA, USA; [4]Mass General Brigham Gene and Cell Therapy Institute, Boston, MA, USA

Dystrophic cardiomyopathy is a significant feature of Duchenne muscular dystrophy (DMD). Increased cardiomyocyte cytosolic calcium (Ca^{2+}) and interstitial fibrosis are major pathophysiological hallmarks that ultimately result in cardiac dysfunction. MicroRNA-25 (miR-25) has been identified as a suppressor of both sarcoplasmic reticulum calcium ATPase 2a (SERCA2a) and mothers against decapentaplegic homolog-7 (Smad7) proteins. In this study, we created a gene transfer using an miR-25 tough decoy (TuD) RNA inhibitor delivered via recombinant adeno-associated virus serotype 9 (AAV9) to evaluate the effect of miR-25 inhibition on cardiac and skeletal muscle function in aged dystrophin/utrophin haploinsufficient mice *mdx/utrn* (+/−), a validated transgenic murine model of DMD. We found that the intravenous delivery of AAV9 miR-25 TuD resulted in strong and stable inhibition of cardiac miR-25 levels, together with the restoration of SERCA2a and Smad7 expression. This was associated with the amelioration of cardiomyocyte interstitial fibrosis as well as recovered cardiac function. Furthermore, the direct quadricep intramuscular injection of AAV9 miR-25 TuD significantly restored skeletal muscle Smad7 expression, reduced tissue fibrosis, and enhanced skeletal muscle performance in *mdx/utrn* (+/−) mice. These results imply that miR-25 TuD gene transfer may be a novel therapeutic approach to restore cardiomyocyte Ca^{2+} homeostasis and abrogate tissue fibrosis in DMD.

INTRODUCTION

Duchenne muscular dystrophy (DMD) is an incurable X-linked disorder that results in the progressive deterioration in skeletal and cardiac muscle function due to mutations of the dystrophin gene. DMD is the most common and severe form of muscular dystrophy, affecting between 1 in 3,500 to 1 in 5,000 live male births.[1] Sufferers typically becoming wheelchair-dependent by adolescence, with high mortality rates in early adulthood due to unremitting disease progression.[2,3] Advances in respiratory support and corticosteroid therapy to reduce muscle inflammation have led to an increased average lifespan, as well as the ambulatory duration of patients with DMD. Consequently,

DMD-related cardiac dysfunction is becoming a more prominent cause of morbidity and mortality, affecting 59% of boys with DMD by 10 years of age and accounting for up to 40% of deaths among all DMD patients.[4,5]

In humans, DMD-related cardiac dysfunction is characterized pathologically by cardiomyocyte hypertrophy and necrosis, ultimately resulting in significant interstitial fibrosis formation.[3,6] Clinically, dystrophic cardiac disease manifests as a dilated cardiomyopathy with thinning of ventricular and septal walls, as well as decreased ventricular ejection fraction and fractional shortening (FS).[3,6] Nearly all types of arrhythmias have been observed and are thought to be a significant cause of mortality.[3,7] Cardiac magnetic resonance imaging typically shows late gadolinium enhancement, which preferentially localizes to the subepicardium of the inferolateral left ventricular wall corresponding to areas of high mechanical stress with subsequent fibrosis and scar formation.[8,9] Interestingly, dystrophin (*mdx*) genetic knockout mice display only a mild form of skeletal dystrophy and do not typically develop cardiac dysfunction until after 15 months of age.[10] Utrophin (*utrn*) is an autosomal paralog of dystrophin and can compensate for dystrophin deficiencies. Combining mdx with *utrn* double knockout (dko) mice results in severe muscle weakness, profound growth restriction, and premature death.[11] The disease severity of the *dko mdx/utrn* (−/−) makes it an impractical experimental model for testing therapeutic modalities. Therefore, an intermediate haploinsufficient model *mdx/utrn* (+/−) was developed, striking an ideal balance whereby significant skeletal muscle inflammation and fibrosis occurs; however, life expectancy is long enough for dystrophic cardiac manifestations to occur while providing adequate time to evaluate novel therapeutics.[10–12]

Correspondence: Dongtak Jeong, PhD, Department of Medicinal & Life Science, College of Science and Convergence Technology, Hanyang University-ERICA, 55 Hanyangdaehak-ro, Sangnok-gu, Ansan 15588, South Korea.
E-mail: cooljdt@hanyang.ac.kr

Interruption of intracellular calcium (Ca^{2+}) cycling is a cardinal feature of cardiac failure at the molecular level.[13,14] Of the many intracellular mechanisms that contribute to Ca^{2+} handling, the sarcoplasmic reticulum ATPase 2a (SERCA2a) has been shown to be the dominant generator of Ca^{2+} re-uptake within cardiomyocytes during diastole. SERCA2a expression levels are decreased in heart failure, and increasing SERCA2a expression via gene transfer therapy improves Ca^{2+} cycling and cardiac function in heart failure mouse models.[15,16] It has previously been shown that SERCA2a mRNA and protein expression is significantly decreased in cardiac tissue of *mdx* mice.[17] Moreover, enhanced SERCA2a expression via gene transfer has previously been shown to improve electrocardiogram (ECG) performance in aged *mdx* mice.[18]

MicroRNAs (miRNAs) are a family of small non-coding RNAs that silence mRNA and regulate gene expression at the post-transcriptional level.[19] Previously, our group identified miR-25 as a significant suppressor of SERCA2a, with pathological upregulation of endogenous miR-25 detected in human myocardial samples obtained from patients with severe heart failure. In the same study, miR-25 inhibition via an antisense oligonucleotide antagomir halted the progression of cardiac dysfunction in mice that underwent *trans*-aortic constriction surgery.[20] The observed abrogation in cardiac dysfunction was thought to be largely due to the restoration of SERCA2a mRNA and protein.[20] The antagomir was delivered systemically using nanoparticle technology, the major limitations of which include poor tissue specificity and very limited duration of effect on the target tissue.

Transforming growth factor β 1 (TGF-β1) is a potent mediator of fibrosis and is elevated in DMD.[21] Mothers against decapentaplegic homolog-7 (Smad7) are endogenous inhibitory Smad proteins that negatively regulate TGF-β signaling.[22,23] Specifically, direct TGF-β antagonism has been a therapeutic strategy employed in previous studies to reduce fibrosis formation in *mdx* knockout (KO) mice.[21–25] In addition, Smad7 has been shown to be a validated target of miR-25, where elevated miR-25 levels result in reduced Smad7 expression.[26–28]

Traditional models of competitive miRNA inhibition such as chemically modified oligonucleotides and Sponge Decoys invariably produce transient miRNA suppression.[29] Inhibitory decoy RNAs expressed in lentiviral vectors have been shown to suppress miRNA with great efficiency and specificity.[29] With further refinement, the optimal arrangement of RNA stem length, miRNA binding sites, and the adjoining linker sequence resulted in a construct coined "tough decoy" (TuD), which has been shown to produce the most potent suppression of miRNA.[29,30] When delivered through a viral vector, TuD RNA conferred the longest duration of miRNA suppression.[31] Among validated viral vectors, adeno-associated virus 9 (AAV9) is highly cardiotropic.[32,33] In this study, we combined the highly proficient TuD miRNA inhibitor against miR-25 with the cardiac-specific AAV9 vector. This AAV9 miR-25 TuD therapy was administered intravascularly via tail vein injection to assess the effects

of miR-25 inhibition on cardiac function in aged *mdx/utrn* (+/−) mice. Given that impaired intracellular Ca^{2+} homeostasis and interstitial fibrosis are the two major hallmarks of DMD-related cardiomyopathy, we hypothesize that strong inhibition of miR-25 may result in improved cardiac function in aged *mdx/utrn* (+/−) mice by restoring SERCA2a and Smad7.

Furthermore, it has previously been shown that the genetic disruption of Smad7 impairs skeletal muscle function with decreased muscle mass, reduced force generation, and delayed recovery from injury.[34] Therefore, we hypothesize that miR-25 TuD transfer into skeletal muscles may enhance muscle performance by restoring Smad7 expression. We performed a treadmill exhaustion test to validate this hypothesis and measured the running distance in *mdx/utrn* (+/−) mice after direct intramuscular AAV9 miR-25 TuD gene transfer.

RESULTS

There is significant upregulation of miR-25 in DMD animal models

We first analyzed the major Ca^{2+} signaling regulators SERCA2a and phospholamban (PLN) by western blot analysis. As shown in Figure 1, SERCA2a and phosphorylated phospholamban (*p*-PLN) expressions were significantly downregulated in both the Muscular Dystrophy in Golden Retriever (GRMD) canine DMD model (Figure 1A, n = 2) and aged *mdx/utrn* (+/−) murine model (Figure 1C, p < 0.005, n = 3). Furthermore, miR-25 expression was measured by qRT-PCR and was found to be substantially upregulated in both models (Figures 1B and 1D, n = 3), confirming a negative relationship with SERCA2a expression.

Cardiac function is compromised in aged *mdx/utrn* (+/–) KO mice

Aged *mdx/utrn* (+/−) mice are shown in Figure 1E. Body weight did not differ between wild-type (WT) mice and *mdx/utrn* (+/−) mice. However, *mdx/utrn* dko mice (−/−) showed a significant reduction in body weight (Figure 1F, n = 15 for each group), as well as spinal deformities resulting in limited mobility and subsequently less feeding. The lifespan of *mdx/utrn* dko mice is less than 6 weeks in the absence of a compensatory supportive device within the caging environment. Functionally, *mdx/utrn* (+/−) mice demonstrate cardiac defects as early as 3 months; however, do not express the severity of skeletal muscle dystrophy and limited lifespan of *mdx/utrn* (−/−) mice.[35–37] To have a consistent functional baseline, we chose to use aged *mdx/utrn* (+/−) mice (more than 9 months old), which were shown to experience cardiac dysfunction with FS values falling below 55% as early as 6 months of age, with a progressive decline shown thereafter (Figure 1G, n = 15 for each group).

AAV9 miR-25 TuD transfer improved cardiac function in aged *mdx/utrn* (+/–) mice
Myocyte contractility and Ca^{2+} transient
To evaluate the effect of miR-25 modulation on cardiomyocyte (CM) contractility, CMs were isolated from AAV9 miR-25 TuD-treated

mouse hearts using the Langendorff system described in the materials and methods section. The contractile properties of isolated CMs were measured using a dual-excitation photomultiplier system (IonOptix). Peak shortening and rates of contraction and relaxation were significantly impaired in CMs isolated from *mdx/utrn* (+/−) mice, which were partially restored in CMs from AAV9 miR-25 TuD-treated hearts (Figure 2A, n = 30 for each group). Furthermore, the amplitudes of Ca^{2+} transients and Tau values, representing the relaxation duration after excitation, were severely impaired in *mdx/utrn* (+/−) mice but were significantly enhanced by miR-25 normalization (Figure 2A, n = 30 for each group).

Echocardiogram results

In the *mdx/utrn* (+/−) group that received the AAV9 miR-25 TuD tail vein injection, the average FS before treatment was 48.58% ± 5.88 (n = 12). This improved to 50.98% ± 5.27 (n = 12) at 4 weeks post-gene transfer and then to 53.75% ± 3.78 (n = 12) at 8 weeks post-gene transfer (Figure 2B, p < 0.005). *mdx/utrn* (+/−) mice which received the AAV9 control injection started with an average FS of 51.68% ± 3.20% (n = 15); however, deteriorated to 47.44% ± 4.48% (n = 15) at 4 weeks post injection, and then deteriorated further to 45.46% ± 3.87% (n = 15) at 8 weeks. Compared with the control, the AAV9 miR-25 TuD transfer resulted in a statistically significant improvement in left ventricular FS (Figure 2B, p < 0.005, n = 15 for each group).

Invasive hemodynamics results

Pressure-volume loop multi-beat analysis post inferior vena cava occlusion showed an average end-systolic pressure-volume relationship (ESPVR) value of 4.04 ± 0.71 (n = 5) in *mdx/utrn* (+/−) mice receiving the AAV9 control. In contrast, the average ESPVR value was 7.26 ± 1.81 (n = 5) in the *mdx/utrn* (+/−) mice that received AAV9 miR-25 TuD transfer, reflecting an improvement in end-systolic elastance and myocardial contractility (p < 0.005). An improvement was also observed in the inotropic responsiveness to dobutamine in aged *mdx/utrn* (+/−) mice treated with AAV9 miR-25 TuD. Averages of the percentage change in peak left ventricular pressure, Tau, maximum left ventricular pressure change during isovolumetric contractile period (dP/dt_{Max}), and heart rate (HR) were recorded post intravenous administration of dobutamine, all of which were enhanced in the AAV9 miR-25 TuD compared with the AAV9 control (Figure 2C, n = 5, p < 0.05), representing an overall improvement in both chronotropic and inotropic competency under stress conditions (Figure 2C).

AAV9 miR-25 TuD transfer improved the overall survival of mdx/utrn (+/–) mice

Mortality rates of *mdx/utrn* (+/−) mice were recorded from birth to 473 days, at which time all animals were euthanized. Intravenous AAV9 miR-25 TuD injection (1E11vg/mouse) was performed at 6 months after birth when cardiac dysfunction was prominent by echocardiography. At the end of the study period, survival rates were 34.4% for mice receiving AAV9 control and 47.7% for mice receiving AAV9 miR-25 TuD (Figure 2D, p < 0.001, n = 20 for

each group). Taken together, the AAV9 miR-25 TuD transfer conferred a survival benefit to *mdx/utrn* (+/−) mice compared with control mice.

AAV9 miR-25 TuD restores Ca^{2+} regulating proteins and reduces cardiac stress markers

The expression of Ca^{2+}-regulating proteins was examined in response to systemic AAV9 miR-25 TuD delivery. Western blot analysis revealed a significant restoration of SERCA2a expression after intravenous AAV9 miR-25 TuD transfer in aged *mdx/utrn* (+/−) mice. The proportion of *p*-PLN/PLN was significantly decreased in *mdx/utrn* (+/−) mice that received the AAV9 control compared with WT mice (Figure 3A, p < 0.005). The *p*-PLN/PLN ratio increased significantly with AAV9 miR-25 TuD transfer (Figure 3A, p < 0.005). No statistically significant differences in ryanodine receptor (RyR) or sodium/potassium exchanger (NCX) expression levels were observed between the WT, *mdx/utrn* (+/−) AAV control, and *mdx/utrn* (+/−) AAV miR-25 TuD-treated mice (Figure 3A). Furthermore, cardiac stress markers atrial natriuretic factor (ANF), brain natriuretic peptide (BNP), α-skeletal α-actin (α-SKA), and beta-myosin heavy chain (β-MHC) were also substantially downregulated by AAV9 miR-25 TuD transfer compared with AAV9 control mice (all p < 0.05, Figure 3B).

AAV9 miR-25 TuD inhibits cardiac mitogen-activated protein kinase signaling

To determine the effect of miR-25 inhibition on cardiac remodeling, several mitogen-activated protein kinase (MAPK) biomarkers were measured using western blot analysis. These include extracellular signal-related kinase (ERK), c-Jun NH2-terminal kinase (JNK), and p38 kinase. We found that aged *mdx/utrn* (+/−) mice treated with AAV9 control had significantly increased expression levels of *p*-ERK/ERK (p < 0.005), *p*-JNK/JNK (p < 0.005), and p-p38/p38 (p < 0.05) compared with WT, which were significantly normalized following AAV9 miR-25 TuD transfer (Figure 4A). Taken together, AAV9 miR-25 TuD transfer resulted in a significant inhibition of MAPK signaling compared with the control.

AAV9 miR-25 TuD transfer inhibits pro-apoptotic signaling pathways

Next, we examined the expression levels of apoptotic biomarkers using western blotting to determine the response to miR-25 inhibition. B cell lymphoma 2 (Bcl-2) expression, a cell-survival signal, was significantly decreased in *mdx/utrn* (+/−) mice that received AAV9 control (p < 0.05). Conversely, Bcl-2 expression was significantly increased in *mdx/utrn* (+/−) mice that received AAV9 miR-25 TuD (Figure 4B, p < 0.005). Bcl-2-associated X (BAX) and cleaved caspase-3 expression, both apoptotic signaling proteins, were shown to be increased in *mdx/utrn* (+/−) mice that received AAV control when compared with WT mice (Figure 4B, p < 0.05 and p < 0.005, respectively), but were both significantly reduced in *mdx/utrn* (+/−) mice that received AAV9 miR-25 TuD transfer (Figure 4B, p < 0.05). Furthermore, we isolated cardiac myocytes and non-myocytes (predominantly fibroblasts) using the Langendorff perfusion
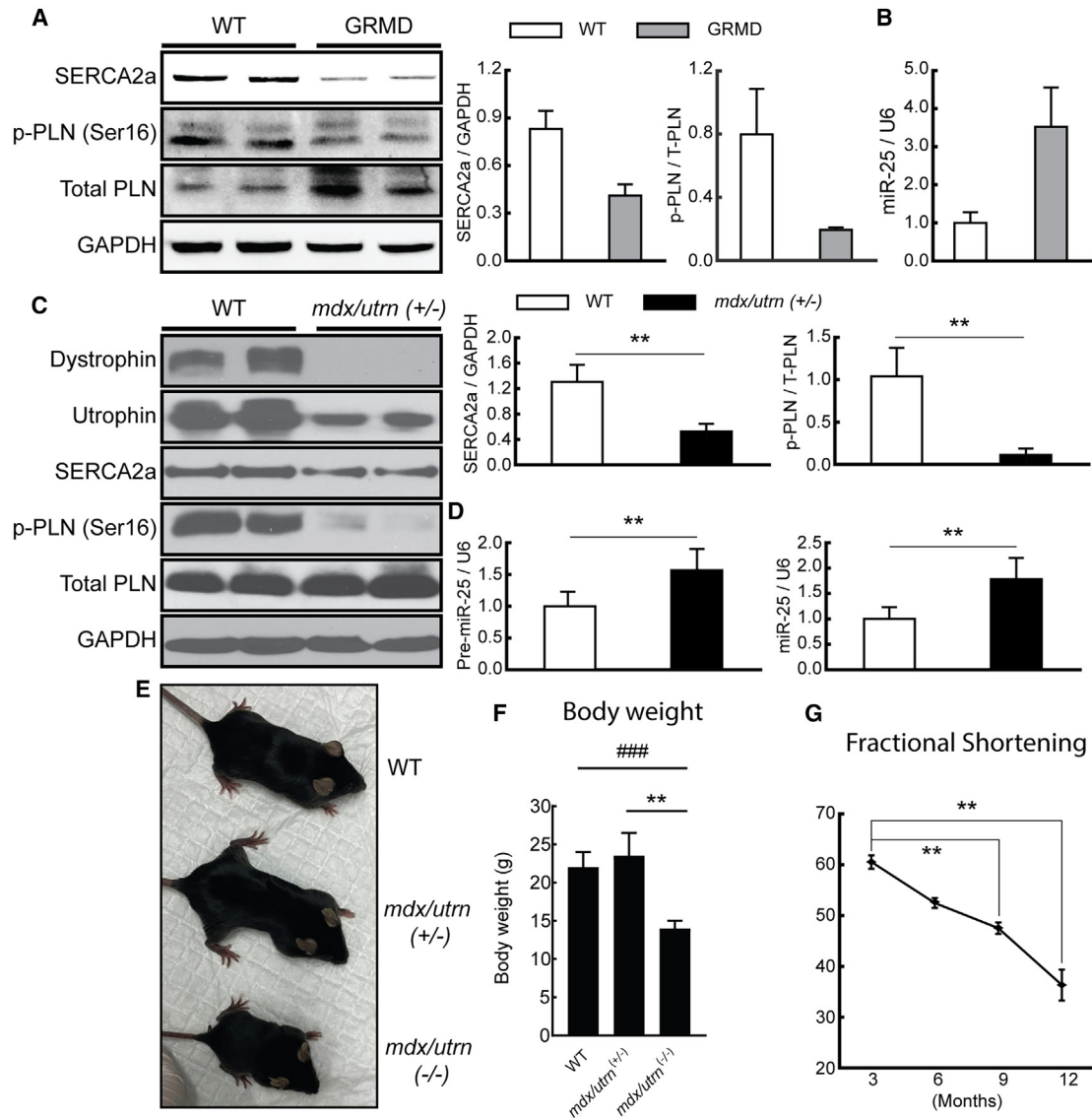
Figure 1. miR-25 is significantly upregulated in DMD animal models and cardiac function is compromised in aged *mdx/utrn* (+/−) KO mice

(A) Western blots were performed against SERCA2a, *p*-PLN, PLN, and GAPDH in the GRMD canine DMD model, kindly provided by Dr. Dongsheng Duan from the University of Missouri. (B) Expression levels of miR-25 were assessed using qRT-PCR analysis. Data are presented as mean ± SD (n = 2 for each group). (C) Western blots were conducted against SERCA2a, *p*-PLN, PLN, and GAPDH in the *mdx/utrn* haploinsufficient DMD mouse model (n = 3 for each group). (D) In addition, qRT-PCR analysis was used to measure mRNA levels of pre-miR-25, and mature miR-25 (n = 3 for each group). (E) The figure displays WT, *mdx/utrn* haploinsufficient (+/−), and *mdx/utrn* double KO (−/−) mouse models, with body weight measured at 2 months of age (F) due to high mortality of dko mice. Cardiac function was assessed in the *mdx/utrn* (+/−) haploinsufficient model using echocardiography over a 1-year period. Fractional shortening was used to represent cardiac function (G). For (F) and (G), n = 15 for each group. In the western blot analysis, 15 μg of proteins was loaded into each well. Data are presented as mean ± SD. *p < 0.05, **p < 0.005.

system to characterize whether the inhibition of pro-apoptotic signaling by AAV9 miR-25 TuD delivery is cell-type specific. As shown in Figure S1, both cell types were commonly inhibited by AAV9 miR-25 TuD transfer. Western blotting results were also confirmed by TUNEL staining of tissue-sectioned specimens (Figure S2). These findings indicated that miR-25 inhibition protects cardiomyocytes from apoptosis by normalizing Ca²⁺ signaling via SERCA2a expression.

Intravenous AAV9 miR-25 TuD transfer decreased cardiac muscle fibrosis in aged *mdx/utrn* (+/−) mice

Histological analyses were performed on frozen cardiac muscle sections from aged *mdx/utrn* (+/−) mice that had received either AAV9 miR-25 TuD or AAV9 Control delivery. Hematoxylin and eosin (H&E) staining of ventricular cardiac muscle from *mdx/utrn* (+/−) AAV9 control mice showed areas of interstitial fibrosis with a greater distance between myocytes, necrotic myofibers with
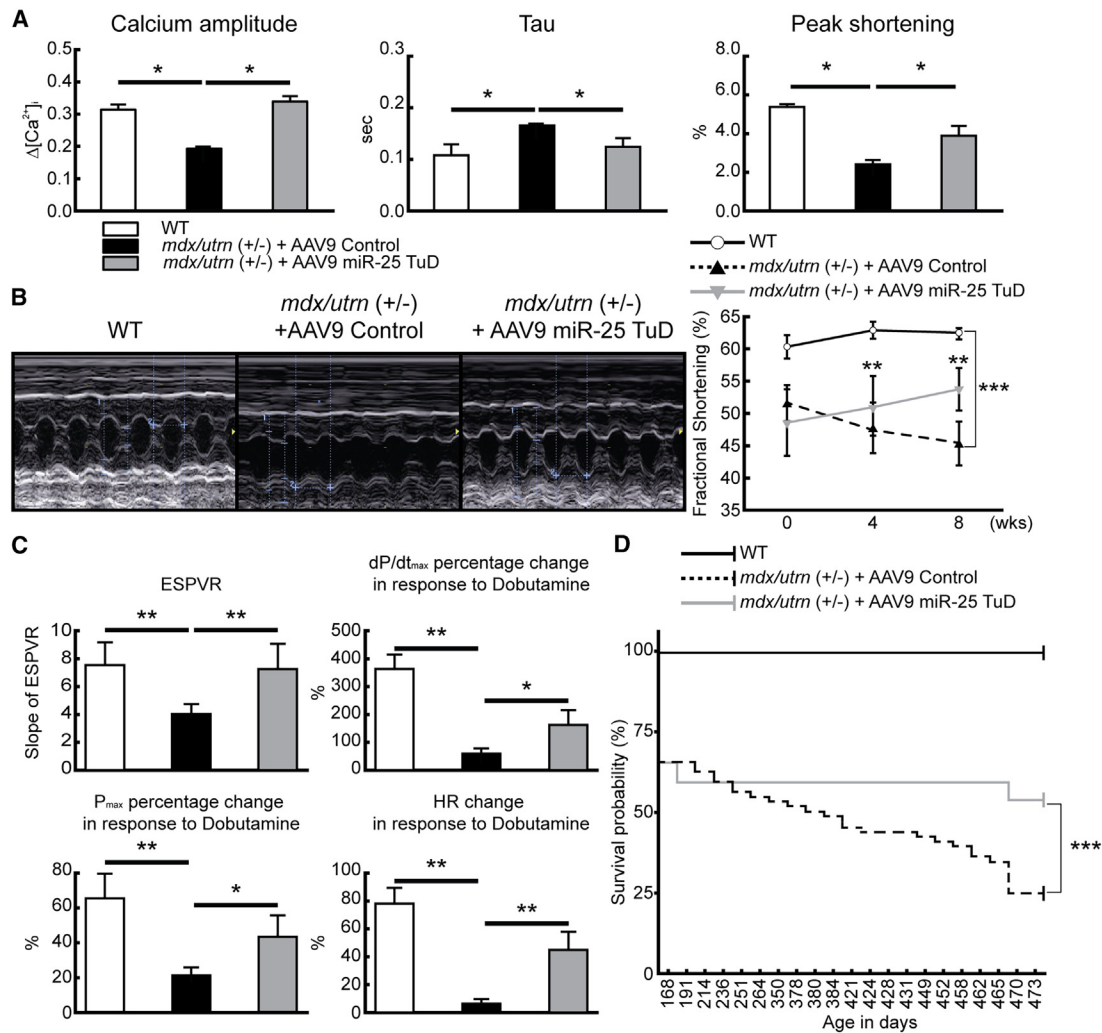
Figure 2. AAV9 miR-25 TuD transfer improved cardiac function in aged *mdx/utrn* (+/−) mice

(A) Cardiomyocytes isolated from WT, AAV9 control treated *mdx/utrn* (+/−), and AAV9 miR-25 TuD-treated *mdx/utrn* (+/−) mice were assessed for Ca^{2+} amplitude, Tau, peak shortening, and maximal rate of contraction and relaxation. AAV9 miR-25 TuD treatment demonstrated enhanced cardiomyocyte Ca^{2+} handling and contractility (n = 30 for each group). (B) Echocardiograms of WT, AAV9 control treated *mdx/utrn* (+/−), and AAV9 miR-25 TuD-treated *mdx/utrn* (+/−) mice were performed after 8 weeks. Notably, AAV9 miR-25 TuD transfer led to a significant improvement in cardiac fractional shortening (n = 15 for each group). (C) Invasive hemodynamic measurements, including ESPVR, and responses to dobutamine through Pmax, Pdt, and HR were assessed in WT, AAV9 control treated *mdx/utrn* (+/−), and AAV9 miR-25 TuD-treated *mdx/utrn* (+/−) mice. AAV9 miR-25 TuD transfer resulted in a substantial improvement in chronotropic and inotropic competency (n = 5 for each group). (D) Survival analysis of WT, AAV9 control treated *mdx/utrn* (+/−), and AAV9 miR-25 TuD-treated *mdx/utrn* (+/−) mice demonstrated a significantly enhanced survival rate for *mdx/utrn* (+/−) mice (n = 20 for each group). For (A)–(D), the data are presented as mean ± SD. *p < 0.05, **p < 0.005, ***p < 0.001.

mononuclear infiltrates, and widespread cellular hypertrophy (Figure 5A). H&E staining of ventricular cardiac muscle from aged *mdx/utrn* (+/−) mice that received AAV9 miR-25 TuD transfer showed a more organized structure with appreciably less interstitial fibrosis, and myocyte sizes similar to those found in WT mice (Figure 5C, p < 0.05). The effectiveness of AAV9 miR-25 TuD treatment was supported by picrosirius red staining, revealing significantly reduced interstitial collagen deposition compared with the control group. In contrast, the control mice exhibited considerable interstitial fibrosis, as indicated by noticeably larger areas of picrosirius red stain-

ing (Figure 5B). Quantitative analysis using ImageJ software confirmed a 70% increase in fibrosis among *mdx/utrn* (+/−) control mice compared with WT mice (Figure 5D, p < 0.005). In contrast, *mdx/utrn* (+/−) mice that received AAV9 miR-25 TuD demonstrated a 40% reduction in fibrosis compared with the controls (Figure 5D, p < 0.005). In addition, we analyzed the ultrastructural phenotype of ventricular cardiomyocytes using transmission electron microscopy. As shown in Figure 5E, *mdx/utrn* (+/−) mice showed greater intracellular disorganization and ultrastructural deterioration compared with WT mice, while AAV miR-25 TuD treatment

demonstrated a degree of cardiomyocyte ultrastructure restoration and, overall, less intracellular disorganization compared with the control.

Smad7 is identified as an essential target of miR-25 in cardiac fibrosis

Given our observed reduction in cardiac fibrosis by AAV9 miR-25 TuD gene transfer, we hypothesized that fibrosis-regulating molecule can be a direct target of miR-25. Therefore, we utilized three miRNA target gene prediction software packages: Target Scan 7.0, miRDB, and PicTar to identify direct targets of miR-25 with respect to fibrosis. As a result, we identified 126 genes predicted to be potential targets of miR-25. We performed additional validation among these targets using Harmonizome 3.0 to confirm their functional relevance. We finally selected four putative candidates: ADM, SERCA2a, DSC2, and Smad7 (Figure 6A). Among these four candidates, Smad7 was of particular interest because it is an endogenous inhibitor of the TGF-β signaling pathway that is associated with fibrosis in diverse organs.[38–42] In addition, we found that Smad7 has a putative binding site between 1314 and 1337 in the 3′untranslated region (3′UTR) with miR-25. Using a luciferase-Smad7-3′UTR reporter assay system, we validated that miR-25 significantly repressed the luciferase activity in a dose-dependent manner. This inhibitory effect was completely abolished when a putative binding site of miR-25 was deleted in the Smad7-3′UTR region (Figures 6A and 6B, p < 0.005).

Moreover, AAV9-mediated miR-25 overexpression reduced Smad7 and SERCA2a expression in WT mouse hearts (Figure 6C). Based on this finding, we characterized the effect of miR-25 TuD, with or without Smad7 expression using a Lenti-shSmad7 viral vector (Figure 6D). Consistent with previous data, the antifibrotic effect of miR-25 inhibition was significantly reduced in the absence of Smad7 expression (Figure 6E). Further histological analysis with Masson's trichrome staining confirmed that cardiac fibrosis was more prominent without Smad7 expression, even after AAV9 miR-25 TuD delivery (Figure 6F). Collectively, these data further validate that Smad7 is a direct target of miR-25.

AAV9 miR-25 TuD reduces fibrosis by inhibiting TGF-β signaling pathways through restoring Smad7 expression

Based on previous results, we first measured the expression level of Smad7 in the animal models of DMD and found that its expression was a dramatically downregulated expression profile in both the canine and mouse models (Figure 7A [n = 2] and C, p < 0.005). Following AAV9 miR-25 TuD treatment in the *mdx/utrn* (+/−) mice, pre- and mature miR-25 expression levels were quantified, and both forms of miR-25 were markedly downregulated (Figure 7B, p < 0.05). Moreover, systemic AAV9 miR-25 TuD delivery in the mouse model significantly restored Smad7 protein expression (Figure 7C, p < 0.005). Smad2 activation (phosphorylation) was also evaluated since it is a critical pro-fibrotic molecule in TGF-β signaling. As shown in Figure S3, Smad2 phosphorylation was substantially reduced by AAV9 miR-25 TuD transfer. Subsequently, other specific fibrotic markers such as fibronectin, galectin-3, and TGF-β1 were also

measured by qRT-PCR and showed significant suppression by AAV9 miR-25 TuD treatment (Figure 7D, p < 0.005). Additionally, several key inflammation markers were also characterized following AAV9 miR-25 TuD transfer using qRT-PCR analysis. We found that pro-inflammatory cytokines such as interleukin (IL)-1b and IL16 were significantly downregulated, while anti-inflammatory cytokines such as IL-4 and IL-10 were substantially increased by AAV9 miR-25 TuD transfer (Figure S4).

Taken together, a marked reduction in pro-fibrotic and pro-inflammatory markers was observed in *mdx/utrn* (+/−) mice treated with AAV9 miR-25 TuD, which is thought to result from restoring Smad7 expression.

Direct intramuscular injection of AAV9 miR-25 TuD improves skeletal muscle performance

Given the prominence of skeletal muscle fibrosis in DMD,[43–46] we sought to evaluate the effect of AAV9 miR-25 TuD gene transfer in skeletal muscle. Although the AAV9 serotype shows the highest tropism for cardiac tissue, it has also been shown to infect skeletal muscle.[47–49] To evaluate this further, we quantified the amount of AAV9 viral particle delivered in both cardiac and skeletal muscle following systemic intravascular delivery. As shown in Figure S5, we found that AAV9 is approximately four times more concentrated in cardiac muscle compared with skeletal muscle following injection. Given these findings that systemic delivery using the AAV9 vector showed lower transduction efficiency in skeletal muscles, we administered a single intramuscular injection of AAV9 control as well as AAV9 miR-25 TuD (1E11 vg/mouse) into the quadriceps on both hind legs of *mdx/utrn* (+/−) mice. Prior to further evaluating skeletal muscle function, we conducted an analysis of AAV9 GFP biodistribution through western blot analysis and viral copy number measurement. Dissecting five different muscles (quadriceps, tibialis anterior, gastrocnemius, soleus, extensor digitorum longus) and four major organs (hearts, lungs, livers, and kidneys) from those mice, we confirmed that AAV transduction is predominantly localized to muscles surrounding the needle tract at the injection site, with minimal expression in other leg muscles (Figure S6). This observation is consistent with previous reports.[50–54] Although some expression was noted in the lungs and liver, the impact on cardiac and skeletal function was minimal with intramuscular injection.

To carry out a non-bias functional evaluation of skeletal muscle, we performed a treadmill exhaustion test using a four-lane rodent treadmill (AccuPacer Treadmill, Omnitech Electronics, Columbus, OH, USA). As shown in Figure 8A, AAV9 miR-25 TuD-injected mice showed a 60% increase in the total running distance compared with AAV9 control-injected mice. Subsequent H&E and picrosirius red staining of skeletal muscle from aged *mdx/utrn* (+/−) mice that received the AAV9 control showed much larger areas of interstitial fibrosis and more necrotic myofibers with mononuclear infiltrates compared with that of WT mice, and which was reduced by AAV9 miR-25 TuD delivery (Figure 8B, n = 8 for each group). In addition,
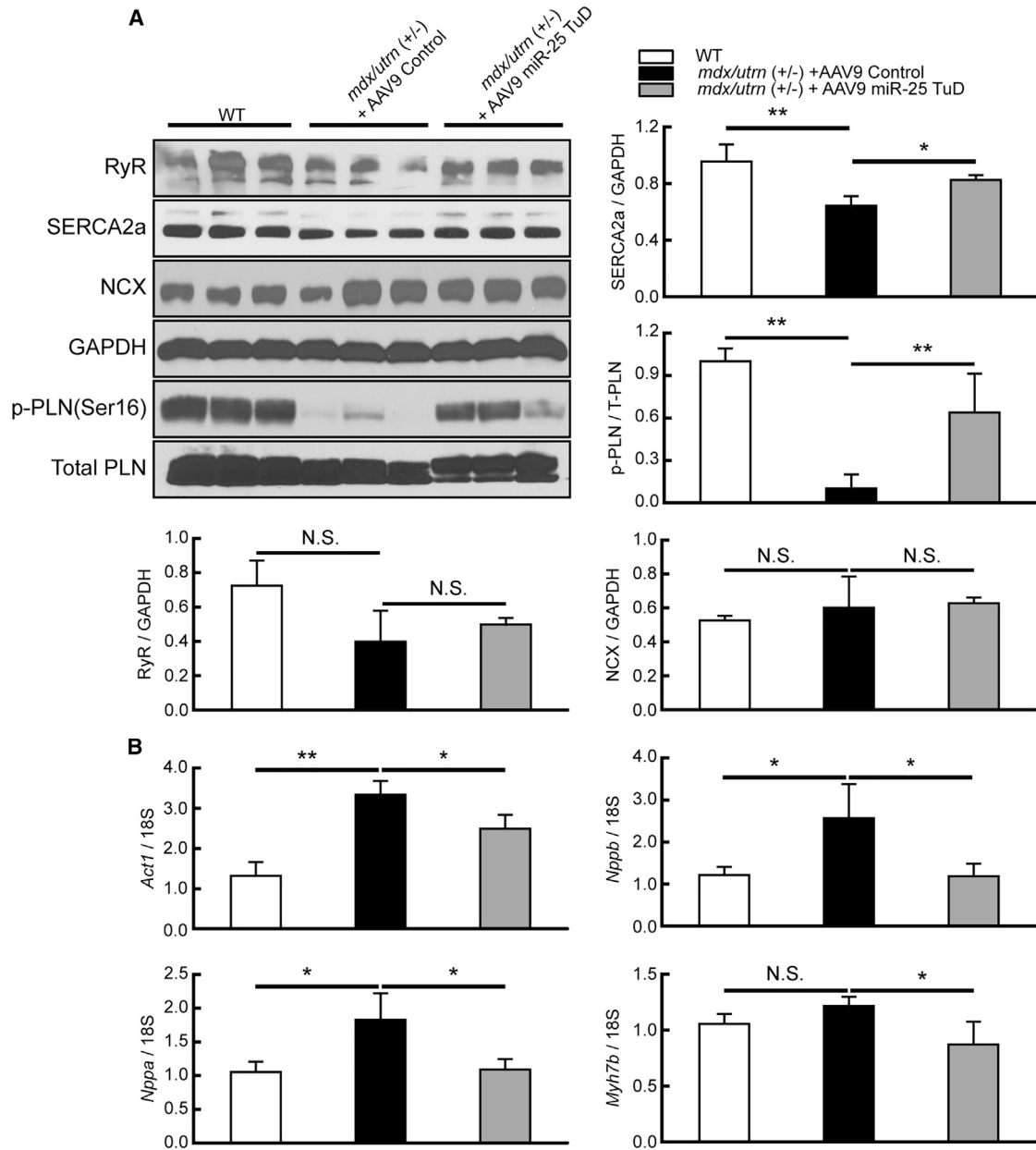
Figure 3. AAV9 miR-25 TuD restores Ca^{2+} regulating proteins and reduces cardiac hypertrophic markers

(A) The expression levels of SERCA2a, phospholamban phosphorylation, RyR, and NCX were analyzed using western blotting in WT, AAV9 control treated *mdx/utrn* (+/−), and AAV9 miR-25 TuD mice. Compared with WT, SERCA2a, and phospholamban phosphorylation levels were significantly downregulated in the AAV9 control group, while both levels exhibited a significant increase with miR-25 decoy transfer. No statistically significant changes were observed in RyR and NCX expression levels (n = 5 for each group). (B) The expression levels of α-SKA, ANF, BNP, and β-MHC were analyzed using qRT-PCR in WT, AAV9 control treated *mdx/utrn* (+/−), and AAV9 miR-25 TuD mice (n = 5 for each group). In the western blot analysis, 20 μg of proteins were loaded into each well. For (A) and (B), the data are presented as mean ± SD. *p < 0.05, **p < 0.005.

we analyzed the ultrastructural phenotype of skeletal muscle using transmission electron microscopy after IM injection (Figure 8C). As shown in Figure 8C, *mdx/utrn* (+/−) mice showed severe myofiber disorganization compared with WT mice. However, AAV9 miR-25 TuD IM treatment resulted in a more organized skeletal muscle ultrastructure compared with the control.

Using these skeletal muscle samples, we analyzed TGF-β and inflammatory signaling pathways by western blot and qRT-PCR analysis. As shown in Figure 8D, pro-fibrotic signaling molecules, such as TGF-β and *p*-Smad2, were downregulated by AAV9 miR-25 TuD delivery, whereas inhibitory Smad7 was upregulated. Fibrotic markers such as vimentin, fibronectin, gelsolin, and α-SMA were also reduced.
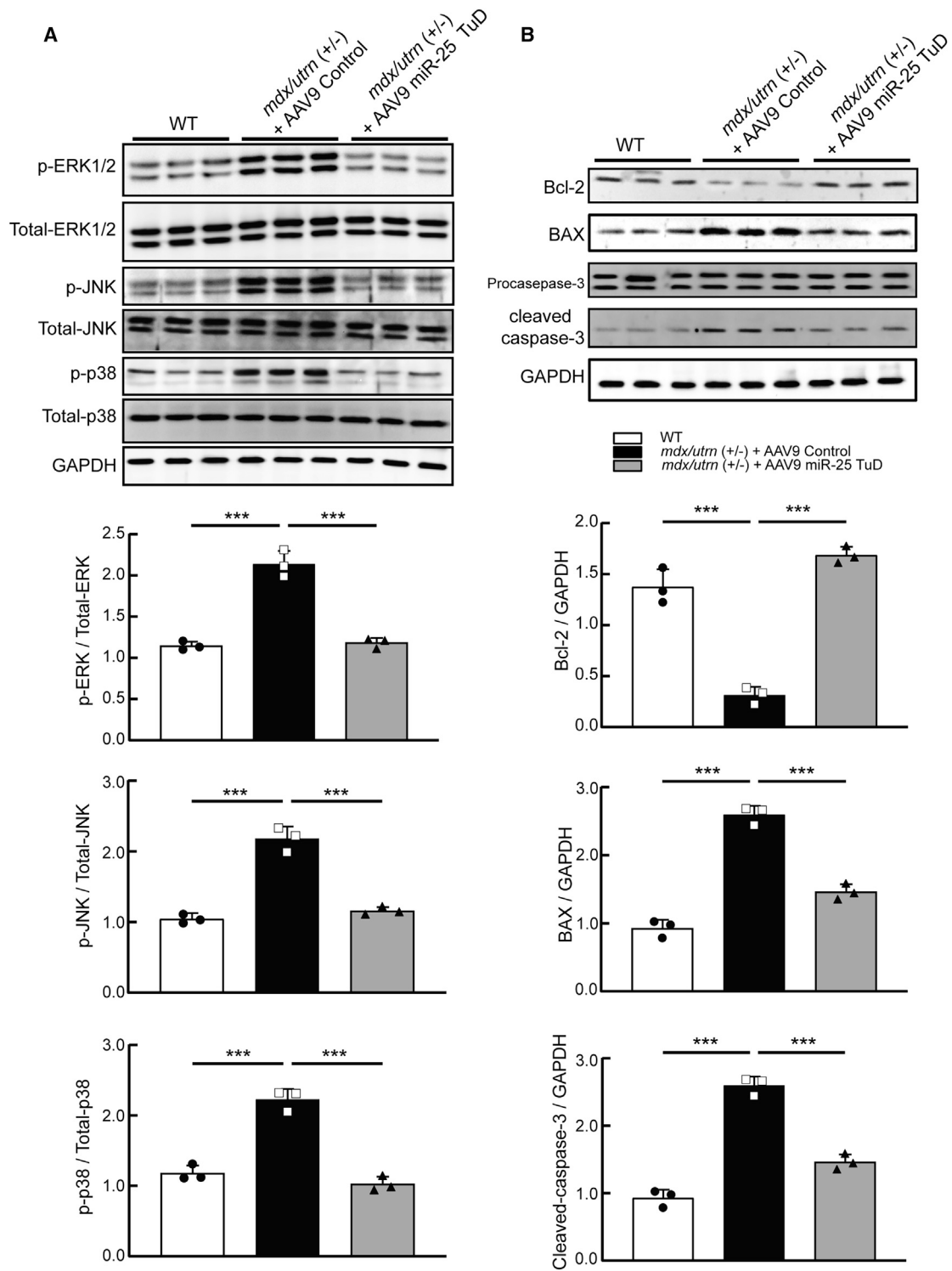
Figure 4. AAV9 miR-25 TuD inhibits cardiac MAPK signaling and pro-apoptotic pathways

(A) The expression levels of MAPK proteins were analyzed by western blotting in WT, AAV9 control treated *mdx/utrn* (+/−), and AAV9 miR-25 TuD mice using the indicated antibodies (n = 5 for each group). (B) The expression levels of apoptosis-related proteins were analyzed by western blotting in WT, AAV9 control treated *mdx/utrn* (+/−), and AAV9 miR-25 TuD mice using the indicated antibodies (n = 5 for each group). In the western blot analysis, 25 μg of proteins was loaded into each well. For (A) and (B), the data are presented as mean ± SD. *p < 0.05, **p < 0.005.
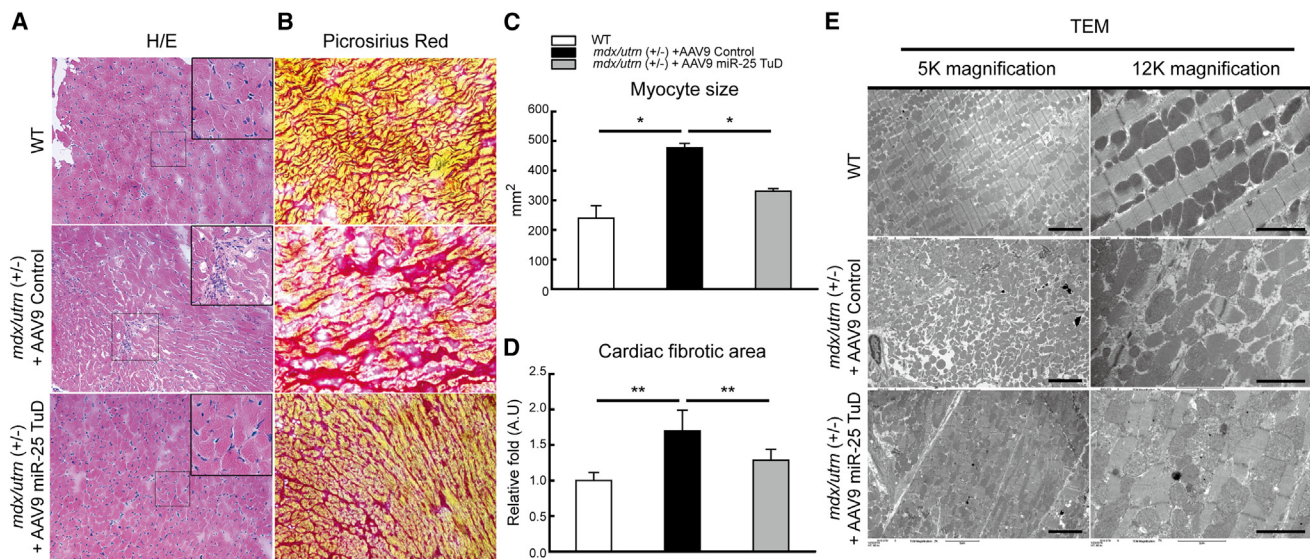
(legend continued on next page)

Figure 5. Systemic AAV9 miR-25 TuD transfer decreased cardiac muscle fibrosis in aged *mdx/utrn* (+/−) mice

Histological analysis was conducted on frozen sections of cardiac muscles obtained from WT, AAV9 control, and AAV9 miR-25 TuD-treated *mdx/utrn* (+/−) mice. (A) Representative images of hematoxylin and eosin (H&E) staining depict cardiac muscles from WT, AAV9 control, or AAV9 miR-25 TuD-treated *mdx/utrn* (+/−) mice. The scale bar indicates 100 μm. (B) Representative images of picrosirius red staining illustrate cardiac muscles from WT, AAV9 control, or AAV9 miR-25 TuD-treated *mdx/utrn* (+/−) mice. The scale bar indicates 100 μm. (C) Quantification of cardiomyocyte size was performed based on H&E staining. (D) Cardiac fibrosis was quantified using picrosirius red staining. (E) Ultrastructural images were obtained using transmission electron microscopy. In the western blot analysis, 15 μg of proteins was loaded into each well. For (C), data are presented as mean ± SD. *$p < 0.05$, **$p < 0.005$ (n = 3 for each group).

Furthermore, both pre- and mature miR-25 expression was successfully reduced by AAV9 miR-25 TuD delivery in skeletal muscles (Figure 8E). Subsequently, pro-inflammatory cytokines such as IL-1b, 6, but not 12 were significantly downregulated, while anti-inflammatory cytokines such as IL-4, 10, and 13 were substantially increased by AAV9 miR-25 TuD treatment compared with the AAV9 control delivered group. (Figures 8F and 8G).

Taken together, AAV9 miR-25 TuD abrogated cardiac dysfunction and fibrosis by upregulating SERCA2a and Smad7 expression. Moreover, direct intramuscular injection of AAV9 miR-25 TuD ameliorated muscular disorganization by inhibiting pro-fibrotic and pro-inflammatory signaling pathways via Smad7 expression in the skeletal muscle, improving muscle performance.

DISCUSSION

DMD has long been considered an attractive target for gene therapy. With packing constraints of 4.7 kb, the AAV vector is incapable of carrying a full-length replacement dystrophin transgene. AAV9 microdystrophin transfer has previously proven ineffective at reducing myocardial fibrosis nor did it improve cardiac function in aged *mdx* mice (>21 months of age) with established dilated cardiomyopathy, suggesting that microdystrophin restoration alone is insufficient to ameliorate established DMD-related cardiac dysfunction.[55] Both anti-oligonucleotide chemistries and readthrough compounds are unable to produce strong cardiac transduction, mostly because of high plasma clearance rates. These therapies are also limited by renal and hepatic toxicities.[56] Therefore, the treatment for dystrophic cardiomy-

opathy is currently limited to pharmacotherapy used for conventional heart failure with variable results.[56] At present, no specific therapeutic strategy exists to reverse the cardiac dysfunction observed in DMD.

Previously, our group successfully generated a TuD RNA inhibitor of miR-25 and combined it with an AAV9 vector system to achieve high cardiac specificity and long-term transgene expression. When the AAV9 miR-25 TuD vector was administered to a pressure overload-induced heart failure model, we were able to demonstrate an amelioration of cardiac dysfunction and tissue fibrosis.[57]

Given that a major pathological hallmark of DMD is aberrations in intracellular Ca^{2+} cycling, together with SERCA2a expression being significantly reduced in multiple DMD mouse models,[58–60] we hypothesized that TuD miR-25 inhibition might rescue DMD-induced cardiomyopathy.

In this respect, we first evaluated the miR-25 expression level in both canine (GRMD) and *mdx/utrn* (+/−) haploinsufficiency mouse models and showed a significant upregulation of miR-25 in both models. Basal characteristic analysis showed that cardiac dysfunction in *mdx/utrn* (+/−) mice could be observed as early as 6 months after birth, and established cardiac fibrosis was observed after 9 months (Figure 1G). Therefore, we decided to perform the therapeutic delivery of AAV9 miR-25 TuD in aged mice (>9 months old).

With reference to cardiac function, we were able to demonstrate that aged *mdx/utrn* (+/−) mice treated with AAV9 miR-25 TuD transfer
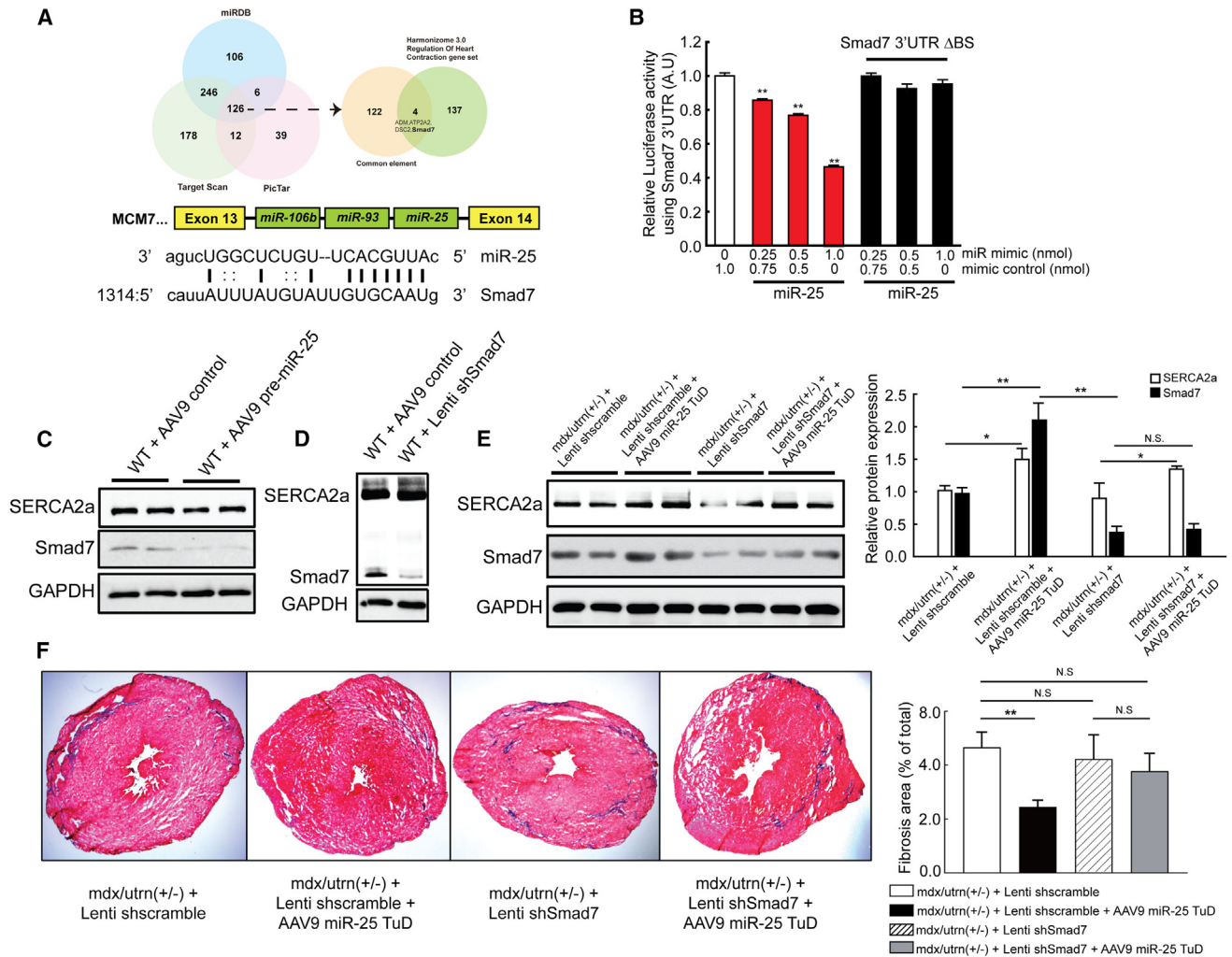
Figure 6. Smad7 is identified as an essential target of miR-25 in cardiac fibrosis

(A) The alignment results between miR-25 and Smad7 3′-UTR provide insights into the specific binding locations within the genome sequence. (B) Luciferase reporter activity was measured using Smad7 3′UTR in a dose-dependent manner with miR-25 mimic. Additionally, a deletion mutation in the miR-25 binding site of Smad7 3′UTR was applied to validate the luciferase activity. Protein levels of SERCA2a and Smad7 were examined by western blot analysis after AAV9 pre-miR-25 delivery in WT mice (C), or lentiviral shSmad7 vector delivery (D). (E) AAV9 miR-25 TuD was injected into *mdx/utrn* (+/−) mice, with or without the lentiviral shSmad7 vector, and protein levels of SERCA2a and Smad7 were detected by western blot analysis. (F) Following euthanasia, mouse hearts were cryosectioned and subjected to Masson's trichrome staining for the evaluation of cardiac fibrosis. In the western blot analysis, 15 μg of proteins was loaded into each well. For (A)–(F), the data are presented as mean ± SD. *p < 0.05, **p < 0.005 (n = 3 for each group).

demonstrated improved cardiomyocyte contractility and Ca^{2+} transient when compared with AAV9 control (Figure 2A). This was validated further with an improved average left ventricular FS (Figure 2B), as well as improvements in invasive hemodynamic parameters together with enhanced chronotropic and inotropic responses to dobutamine-induced stress (Figure 2D).

Furthermore, multiple miRNA target prediction software identified four targets of miR-25 with the most functional relevance to heart contraction. One of the most potent targets with the highest scores was Smad7. Interestingly, Smad7 is a well-characterized anti-fibrotic

molecule in the TGF-β signaling pathway, and genetic disruption of Smad7 impairs skeletal muscle growth and regeneration.[34] Since SERCA2a and Smad7 both play roles in several pathogenic mechanisms related to dystrophic cardiomyopathy and are negatively regulated by miR-25, we rationalized that the effective inhibition of miR-25 would have a beneficial effect on both cardiac and skeletal functions in this DMD mouse model.

Our results showed that the combination of AAV9 miR-25 TuD was a potent suppressor of cardiac and skeletal miR-25 levels, as determined by qRT-PCR (Figures 7B and 8E). This was also correlated with a
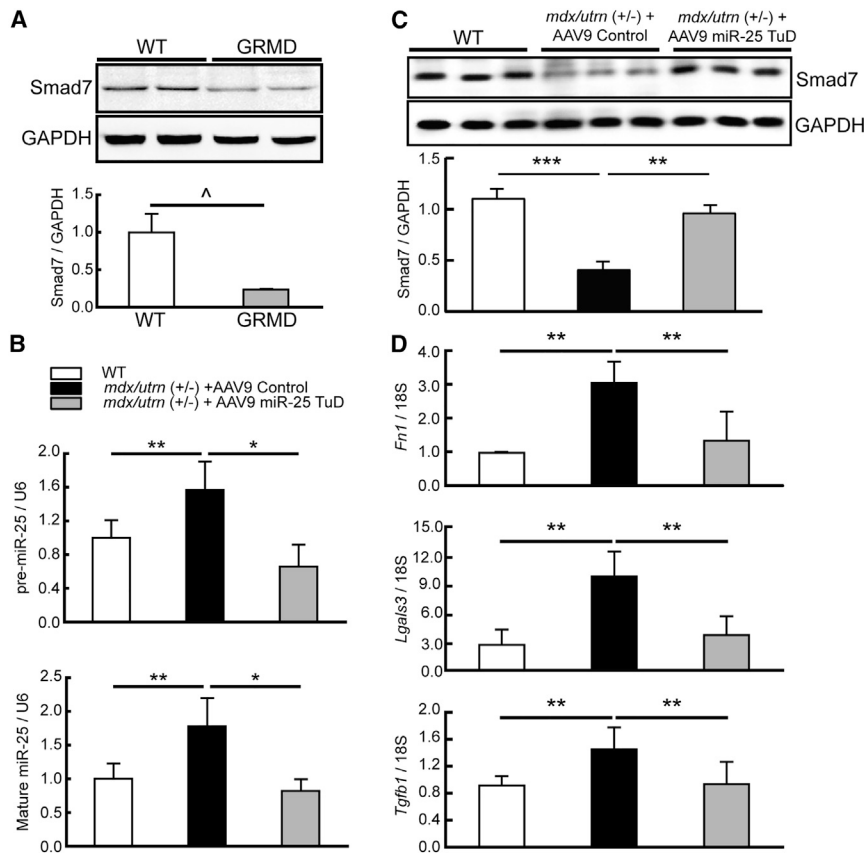
Figure 7. AAV9 miR-25 TuD reduces fibrosis by inhibiting TGF-β signaling pathways by restoring Smad7 expression

Western blotting was performed to evaluate the expression of Smad7 and GAPDH in the canine (GRMD) models (A), with n = 2 for each group. Similarly, in the *mdx/utrn* (+/−) mouse models, western blot analysis was conducted to assess Smad7 and GAPDH expression (B), with n = 5 for each group. (C) The expression levels of pre- and mature miR-25 were quantified using qRT-PCR in *mdx/utrn* (+/−) mice treated with AAV9 control or AAV9 miR-25 TuD, with n = 5 for each group. (D) Furthermore, qRT-PCR analysis was employed to analyze the mRNA expression levels of fibrosis markers, such as fibronectin, galectin-3, and TGF-β1, in comparison with the WT group. In the western blot analysis, 20 μg of proteins was loaded into each well. For (A)–(D), the data represent the mean ± SD. *p < 0.05, **p < 0.005, ***p < 0.001.

the reduced expression of both pro-apoptotic and cardiac stress markers (Figure 3B). Furthermore, we observed significantly lower levels of BCL-2 expression in *mdx/utrn* (+/−) control mice than in WT mice (p < 0.05). This significantly increased after AAV9 miR-25 TuD treatment (Figure 4B, p < 0.005). Conversely, both BAX and cleaved caspase-3 were significantly elevated in the AAV9 control arm compared with WT mice (p < 0.05, p < 0.005, respectively); however, both were significantly reduced in response to AAV9 miR-25 TuD transfer (Figure 4B, p < 0.05).

subsequent increase in total SERCA2a and Smad7 expression levels (Figures 3A, 7C, and 8D).

Much of the DMD phenotype is due to the replacement of healthy myocytes with fibrotic material in both cardiac and skeletal muscles. First, we found that *mdx/utrn* (+/−) mice treated with AAV9 miR-25 TuD transfer had restored cardiac Smad7 expression, together with a significant reduction in the mRNA expression levels of pro-fibrotic biomarkers such as fibronectin, galectin-3, and TGF-β1 (Figure 7D, p < 0.005). This was confirmed histologically by a visible reduction in interstitial cardiac fibrosis and fewer areas of necrosis seen in sections from *mdx/utrn* (+/−) mice that received AAV9 miR-25 TuD transfer compared with the AAV9 control (Figure 5A).

The vulnerability of dystrophin-deficient muscle fibers to mechanical stress has been shown to stimulate MAPK pathways and catalyze progression to cardiac hypertrophy.[61] Compared with WT mice, we found increased expression of MAPK biomarkers in *mdx/utrn* (+/−) control mice, which correlates with previous work.[62,63] Impressively, AAV9 miR-25 TuD transfer resulted in significant reductions in *p*-ERK/ERK (p < 0.005), *p*-JNK/JNK (p < 0.005), and p-p38/p38 (p < 0.005) compared with the control (Figure 4A). This was further validated by the finding that AAV9 miR-25 TuD transfer resulted in

In our routine characterization of target protein expression in disease-related *in vitro* and *in vivo* models through western blot analysis, the careful selection of a stable protein loading control is essential for accurate evaluation. Despite reports suggesting potential variations in the expression levels of common internal loading controls like actin and tubulin under specific disease conditions,[64] we confirmed the stability of these housekeeping proteins in our model, both with and without AAV9 delivery (Figure S7).

Moreover, a significant limitation of AAV therapy is the off-target expression of the target gene.[65,66] To address this concern, various groups have explored novel approaches, such as employing tissue-specific promoters or capsid engineering methods.[67–69] However, these strategies often exhibit reduced transduction efficiency in practical applications.[70,71] In this respect, we utilized an AAV vector containing the typical CMV promoter in our study. Nevertheless, for enhanced clinical applications, there is a need to develop a novel AAV vector with minimal off-target expression.

In summary, we believe that our findings reflect a significant cardiomyocyte survival benefit and protection from pathological cardiac
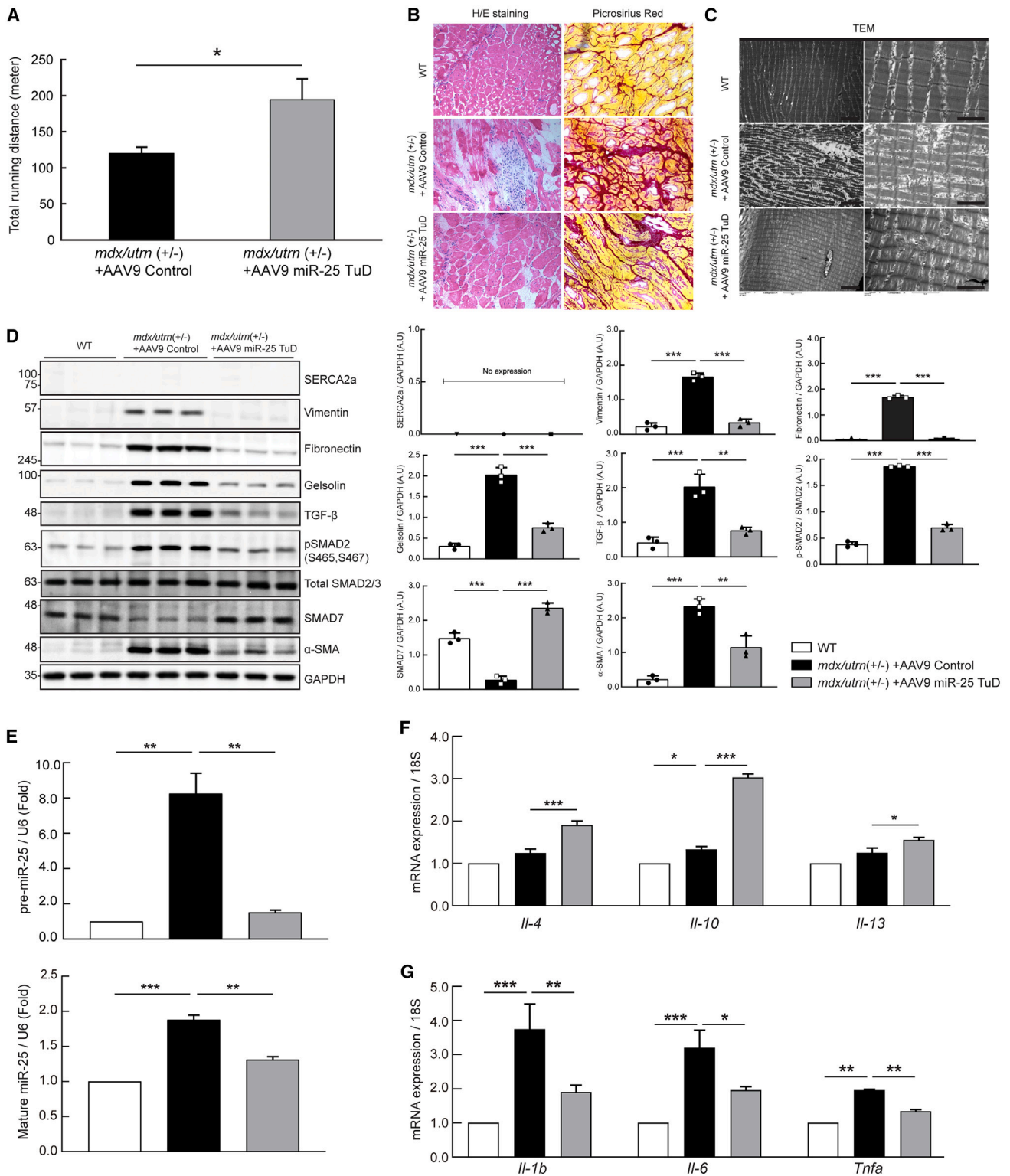
Figure 8. Direct intramuscular injection of AAV9 miR-25 TuD improves muscle performance

(A) The treadmill exhaustion test involved calculating the average running distance on the treadmill during the exercise program. The bars represent the mean values for each group, with error bars indicating the standard deviation (n = 8 for each group). (B) Representative histological images with H&E and picrosirius red staining depict

(legend continued on next page)

remodeling due to the strong inhibition of miR-25 as the restoration of SERCA2a plays a critical role in improving Ca^{2+} handling and contractile properties. Additionally, the increase in Smad7 expression due to miR-25 inhibition appears to abrogate the development of skeletal fibrosis through impeding TGF-β signaling pathways. To evaluate the effect of miR-25 inhibition in skeletal muscles, an additional direct intramuscular injection was administered because systemic delivery using the AAV9 vector showed minimal transduction efficiency in skeletal muscles owing to the cardiotropic nature of AAV9. As shown in Figure 8A, the AAV9 miR-25 TuD-transfected group showed significantly enhanced running performance in the treadmill exhaustion test. This was confirmed histologically by a visible reduction in skeletal muscle fibrosis and disorganization of myofibrils. Moreover, fewer areas of necrosis were observed in sections from *mdx/utrn* (+/−) mice that received the AAV9 miR-25 TuD transfer compared with the AAV9 control. Additional molecular pro-fibrotic markers confirmed that AAV9 miR-25 TuD delivery ameliorated tissue fibrosis and inhibited TGF-β signaling through the restoration of Smad7 expression (Figure 8D).

In an era of a rapidly expanding appreciation of epigenetics, miRNA inhibition has proven to be an increasingly influential method for gene modulation.[71] Our study extends the current understanding in this area by highlighting the influence of miR-25 on dystrophic cardiac dysfunction. This study also successfully demonstrated gene transfer in a DMD model through the refined union of a proficient miRNA inhibitor and a highly cardiotropic viral vector to maximize the efficiency and duration of transgene expression. We believe this demonstration has broader implications, as numerous cardiac miRNA targets have been identified and linked with pathological processes; however, to date, they have largely been studied using chemically modified oligonucleotide inhibitors.[71–75] With much of the focus of DMD gene therapy currently directed toward dystrophin restoration, our study provides additional insights into the utility of miRNA modulation as a potential therapeutic adjunct that specifically targets the cardiac and skeletal muscle dysfunction seen in dystrophic disease.

MATERIALS AND METHODS

Animal care
All procedures were approved by and performed in accordance with the Institutional Animal Care and Use Committee of the Icahn School of Medicine at Mount Sinai (Animal protocol NO.: IACUC-2017-0431 and IACUC-2019-0027). This study conformed to the Guide for the Care and Use of Laboratory Animals published by the US National Institutes of Health (NIH Publication Nos. 85–23, revised 1996). C57BL/10ScSn (Dmd^mdx/Utrn^tm1Jrs) mice were purchased from The Jackson Laboratory (Bar Harbor, ME, USA). Furthermore,

to ensure an authentic dystrophic cardiomyopathy model, only aged *mdx/utrn* (+/−) mice (≥9 months) were included in our study.

AAV9 and lentiviral vector production
Self-complementary adeno-associated virus (AAV, serotype 9) constructs were generated using the pds-AAV2-EGFP vector and the optimal TuD sequence against human miRNA-25, which was kindly donated by Dr. Brian Brown, Professor of Genetics at the Icahn School of Medicine, Mount Sinai. The specificity of the miR-25 TuD was determined through a pMirTarget vector containing Smad7 3′UTR under luciferase (Origene, MD, USA). The eGFP sequence was removed from the AAV construct due to viral packaging constraints, and recombinant AAV was produced by transfecting 293 T cells as described previously.[33] AAV particles in the cell culture media were collected by precipitation with ammonium sulfate and purified by ultracentrifugation on an iodixanol gradient. Using a centrifugal concentrator, the particles were then concentrated by exchanging iodixanol with lactated Ringer's solution in multiple dilution and concentration steps. The AAV titer was determined by quantitative real-time PCR and sodium dodecyl sulfate-polyacrylamide gel electrophoresis, and AAV9 GFP was used as a control. In the cardiac study, 1E11vg of AAV9 was administrated intravenously via tail vein. In the skeletal muscle function analysis, an equivalent amount of AAV9 was intramuscularly injected into the quadricep of both legs. To inhibit Smad7 *in vitro* and *in vivo*, a shLentivirus against Smad7 was purchased from OriGene (Cat No. TL514317V; MD, USA).

Transthoracic echocardiography and *in vivo* hemodynamics
Mice were anesthetized by intraperitoneal injection of ketamine (100 μg/g). Two-dimensional images and M-mode tracings were recorded in the short axis at the left ventricular papillary muscle level using a 15.0 MHz transducer to determine the percentage of FS and ventricular dimensions (GE Vivid 7 Vision; GE Healthcare, Chicago, IL, USA). To improve experimental precision, the same technician performed an ECHO examination throughout the experimental period. Furthermore, a minimum HR of 550 beats per min was required to improve the experimental accuracy to include structural and functional measurements to minimize bradycardia-related underestimations of cardiac function. Measurements were performed at least three times for each mouse, and the average of the measurements was used.

In vivo hemodynamic analysis was performed using a 1.2-Fr pressure-volume (PV) conductance catheter (Scisense, Ontario, Canada). Mice were anesthetized by intraperitoneal injection of a mixture of urethane (1 mg/g), etomidate (10 μg/g), and morphine (1 μg/g), and were then intubated via a tracheotomy and mechanically ventilated

mononuclear infiltrates and tissue fibrosis. The scale bar indicates 100 μm. (C) Ultrastructural images were obtained using transmission electron microscopy. (D) Representative western blot images evaluating markers such as SERCA2a for cardiac calcium pump, vimentin, fibronectin, and gelsolin for fibrosis, TGF-β1, p-Smad2, total Smad2/3, and Smad7 for TGF-β signaling molecules, and α-SMA for myofibroblast (n = 3 for each group). (E) Pre- and mature forms of miR-25 were measured before and after gene transfer (n = 5 for each group). The mRNA expressions for (F) anti-inflammatory and (G) pro-inflammatory cytokines were measured using the qRT-PCR method in skeletal muscles (n = 5 for each group). In the western blot analysis, 20 μg of proteins was loaded into each well. For (A)–(G), the data are presented as mean ± SD. *p < 0.05, **p < 0.005, ***p < 0.001.

at a tidal volume of 7 µL/g and 125 respirations/min. The PV catheter was placed in the left ventricle via an apical stab approach as previously described.[76] The pressure-volume data were analyzed using IOX2 software (EMKA Technologies, Paris, France). Moreover, a cardiac stress challenge was performed by infusing dobutamine at increasing strengths of 1 µg/mL, 10 µg/mL, 100 µg/mL, and 1 mg/mL, each mixed with normal 0.9% saline and delivered via a central venous catheter inserted into the right jugular vein with 10-min wash-out periods between infusions allowing for hemodynamic parameters to normalize.

Histological examination of cardiac and skeletal muscle tissues

Mouse heart tissues were cryopreserved with an optimum cutting temperature compound (Tissue-Tek O.C.T. Compound; Sakura, Torrance, CA, USA) and sectioned into 6-µm-thick slices. To measure cell size, a hematoxylin/eosin (H&E) staining kit (9990001; Fisher Scientific, Hampton, NH, USA) was used to stain the sectioned hearts. The cells were stained pink, and the nuclei were blue. The cross-sectional area was imaged using light microscopy (E400; Nikon, Tokyo, Japan) and analyzed using ImageJ software (NIH) at ×40 magnification. A minimum of 150 cardiomyocytes were measured per heart. To measure the fibrotic areas, a Masson trichrome staining kit (ab150686; Abcam, Trumpington, Cambridge, UK) was used to stain the sectioned hearts. The fibrotic area was stained blue, and the normal tissue was stained red. Finally, the fibrotic area was calculated as the ratio of the total area of fibrosis to the total area of the section using ImageJ software.

Adult primary cardiomyocytes isolation

Cardiomyocytes were isolated from either C57/BL6 WT mouse or *mdx/utrn* (+/−) haploinsufficient mouse hearts, as previously described,[77] with minor modifications. Male mice of 9–12 months of age were included in this study. Briefly, after heparin (50 U) injection, animals were anesthetized with intraperitoneal ketamine (100 mg/g). The heart was quickly removed from the chest, and the aorta was retrogradely perfused at 37°C for 3 min with calcium-free Tyrode buffer (137 mM NaCl, 5.4 mM KCl, 1 mM MgCl$_2$, 10 mM glucose, 10 mM HEPES [pH 7.4], 10 mM 2, 3-butanedione monoxime, and 5 mM taurine) gassed with 100% O$_2$. Subsequently, enzymatic digestion was initiated by adding type B collagenase (300 U/mL; Worthington, Lakewood, NJ, USA) and hyaluronidase (0.1 mg/mL; Worthington, Lakewood, NJ, USA) to the perfusion solution. When the heart became swollen after 10 min of digestion, the left ventricle was quickly removed, cut into several sections, and further digested in a shaker (60–70 rpm) for 10 min at 37°C in the same enzyme solution. The cell suspension was filtered through a cell strainer (100 µm pore size; BD Falcon, Glendale, AZ, USA) and gently centrifuged at 500 rpm for 1 min. Extracellular Ca^{2+} was added back to a concentration of 1.25 mM over 30 min to avoid the Ca^{2+} paradox. This procedure usually yields approximately 80% of viable rod-shaped ventricular myocytes with clear sarcomere striations. Finally, isolated cardiomyocytes were plated onto a laminin-coated plate and cultured in modified Eagle's medium with Hanks' balanced salt solution supplemented with 2 mM L-carnitine, 5 mM creatine, 5 mM taurine, and 100 IU/mL penicillin.

Ca^{2+} transient and contractility measurement

Cardiomyocytes were isolated as described in the myocyte isolation method section. Furthermore, isolated cardiomyocytes were plated on laminin-coated coverslips and stabilized for 2 h, and the mechanical properties of ventricular myocytes were assessed using a video-based edge detection system (IonOptix, Westwood, MA, USA). Cardiomyocytes were stimulated to contract at a frequency of 1 Hz. Changes in sarcomere length were captured and analyzed using soft-edge software (IonWizard, MA, USA). To detect intracellular Ca^{2+} changes, cardiomyocytes were loaded with 0.5 µmol/L Fura2-AM (Life Technologies, Carlsbad, CA, USA), a Ca^{2+}-sensitive indicator, for 10 min at 37°C. Fluorescence emissions were simultaneously recorded using an IonOptix with contractility measurements.

Treadmill (exhaustion test)

Mouse treadmill exercises were performed as previously described.[78] Briefly, 4 weeks after gene transfer, *mdx/turn* (+/−) mice were subjected to a single exercise session on a rodent treadmill. Specifically, the treadmill speed was initially set at 5 m/min, and the mice were acclimated to this condition before running for 5 min at high speeds to avoid injury and potential data artifacts. Subsequently, the treadmill speed was increased by 1 m/min every minute until the mice were not able to return to the track despite the electric shock. The total running distance was calculated precisely for all speeds and durations.

Western blot analysis

Membrane and tissue homogenates were prepared as previously described.[20] Proteins were resolved on 10% sodium dodecyl sulfate-polyacrylamide gel electrophoresis and transferred to PVDF membranes (Millipore, Burlington, MA, USA). An equivalent amount of protein samples was loaded into each well. Protein bands were detected using standard laboratory protocols. The antibody raised against SERCA2a was obtained from 21st Century Biochemicals. In addition, transferred blots were blocked with 5% non-fat skim milk and incubated with antibodies against phospholamban (PLN), *p*-PLN (Badrilla, Leeds, UK), a-SMA (Sigma-Aldrich, Saint Louis, MO, USA), fibronectin (Proteintech, Chicago, IL, USA), Vimentin, Gelsolin, pSmad2, total Smad2/3, TGF-β 1 p-JUN, total-JUN, *p*-ERK, total ERK1/2, p-38, total p-38, caspase3, GAPDH (Cell Signaling, Danvers, MA, USA), Smad7, Bcl-2 (SCBT, Dallas, TX, USA), BAX, NCX (abcam, Trumpington, Cambridge, UK), and cTnT (Novus, Centennial, CO, USA) for 12–16 h at 4°C. The blots were washed with Tris-buffered saline containing 0.1% Tween 20 (TBS-T), incubated with secondary antibodies conjugated to horseradish peroxidase (#31430; Thermo Fisher Scientific, Waltham, MA, USA), and washed again. The band signal was developed using a chemiluminescent solution (#WBKLS0500; Millipore, Burlington, MA, USA). ImageJ plug-in software was used to quantify the western blot results.

Quantitative real-time PCR

Transcript levels were determined by real-time PCR using a QuantiTect SYBR Green Real-Time PCR Kit (Qiagen, CA, USA). Total RNA was isolated from the samples using the TRIzol reagent (Gibco BRL, CA, USA) according to the manufacturer's instructions. Reverse transcription was performed at $50°C$ for 20 min, and cDNA was amplified in 20-μL reaction volumes using 10 pmol of primers for 35 cycles: $94°C$ for 10 s, $57°C$ for 15 s, and $72°C$ for 5 s. 18S RNA was used as an internal control to calculate the relative abundance of the mRNAs. The qPCR primers used in this study are listed in Table S1.

In silico approach to identify miR-25 targets

To predict the targets of microRNA-25-3p (miR-25-3p), we retrieved data from TargetScan (TargetScanHuman 7.0) miRDB (http://www.mirdb.org/, accessed on 21 Mar 2021) and PicTar databases. Subsequently, we employed DAVID to classify the genes from each database based on the disease classes. Next, we compared the target genes identified in each database with the gene set list of cardiac contraction genes in the Harmonizome3.0 database. Using Jvenn, we created a Venn diagram to visualize overlapping genes.

Transmission electron microscopy

Cells and fractions ($1 mm^3$) from fresh ventricles were pre-fixed in a solution of 3% glutaraldehyde overnight at $4°C$, post-fixed in 1% osmium tetroxide (OsO4), dehydrated in an ascending series of alcohols, and embedded in an epoxy resin. Next, the ultrathin sections were stained with uranyl acetate and lead citrate. Furthermore, samples were viewed under a transmission electron microscope (H-7650; Hitachi, Tokyo, Japan), and images were taken at 5 K and 12 K magnification.

Statistical analysis

Statistical analyses were conducted utilizing Student's t test, with significance denoted by a single asterisk (*) representing $p < 0.05$, a double asterisk (**) indicating $p < 0.005$, or a triple asterisk (***) indicating $p < 0.001$. Data are presented as mean ± SD.

Statistical significance was determined using a two-way ANOVA followed by Tukey's test. No adjustments were made for multiple comparisons across the variables tested.

DATA AND CODE AVAILABILITY

Data are available from the corresponding authors on reasonable request.

SUPPLEMENTAL INFORMATION

Supplemental information can be found online at https://doi.org/10.1016/j.omtn.2024.102174.

AUTHOR CONTRIBUTIONS

Conceptualization, D.J.; Methodology, D.J. and S.V.K.; Investigation, S.V.K., J.Y., J.G.O., M.P., C.L., and D.J.; Writing – Original Draft, S.V.K. and D.J.; Writing – Review and Editing, S.V.K. and D.J.; Project Administration, D.J. and S.V.K.; Funding Acquisition, D.J.; Resources, D.J.; Supervision, R.J.H., M.M., and D.J.

DECLARATION OF INTERESTS

The authors declare no competing interests.

REFERENCES

1. Chung, J., Smith, A.L., Hughes, S.C., Niizawa, G., Abdel-Hamid, H.Z., Naylor, E.W., Hughes, T., and Clemens, P.R. (2016). Twenty-year follow-up of newborn screening for patients with muscular dystrophy. Muscle Nerve 53, 570–578. https://doi.org/10.1002/mus.24880.

2. Falzarano, M.S., Scotton, C., Passarelli, C., and Ferlini, A. (2015). Duchenne Muscular Dystrophy: From Diagnosis to Therapy. Molecules 20, 18168–18184. https://doi.org/10.3390/molecules201018168.

3. Spurney, C.F. (2011). Cardiomyopathy of Duchenne muscular dystrophy: current understanding and future directions. Muscle Nerve 44, 8–19. https://doi.org/10.1002/mus.22097.

4. Finsterer, J., and Cripe, L. (2014). Treatment of dystrophin cardiomyopathies. Nat. Rev. Cardiol. 11, 168–179. https://doi.org/10.1038/nrcardio.2013.213.

5. McNally, E.M., Kaltman, J.R., Benson, D.W., Canter, C.E., Cripe, L.H., Duan, D., Finder, J.D., Groh, W.J., Hoffman, E.P., Judge, D.P., et al. (2015). Contemporary cardiac issues in Duchenne muscular dystrophy. Working Group of the National Heart, Lung, and Blood Institute in collaboration with Parent Project Muscular Dystrophy. Circulation 131, 1590–1598. https://doi.org/10.1161/CIRCULATIONAHA.114.015151.

6. Mavrogeni, S., Markousis-Mavrogenis, G., Papavasiliou, A., and Kolovou, G. (2015). Cardiac involvement in Duchenne and Becker muscular dystrophy. World J. Cardiol. 7, 410–414. https://doi.org/10.4330/wjc.v7.i7.410.

7. Romfh, A., and McNally, E.M. (2010). Cardiac assessment in duchenne and becker muscular dystrophies. Curr. Heart Fail. Rep. 7, 212–218. https://doi.org/10.1007/s11897-010-0028-2.

8. Dittrich, S., Tuerk, M., Haaker, G., Greim, V., Buchholz, A., Burkhardt, B., Fujak, A., Trollmann, R., Schmid, A., and Schroeder, R. (2015). Cardiomyopathy in Duchenne Muscular Dystrophy: Current Value of Clinical, Electrophysiological and Imaging Findings in Children and Teenagers. Klin. Pädiatr. 227, 225–231. https://doi.org/10.1055/s-0034-1398689.

9. Verhaert, D., Richards, K., Rafael-Fortney, J.A., and Raman, S.V. (2011). Cardiac involvement in patients with muscular dystrophies: magnetic resonance imaging phenotype and genotypic considerations. Circ. Cardiovasc. Imaging 4, 67–76. https://doi.org/10.1161/CIRCIMAGING.110.960740.

10. Chun, J.L., O'Brien, R., and Berry, S.E. (2012). Cardiac dysfunction and pathology in the dystrophin and utrophin-deficient mouse during development of dilated cardiomyopathy. Neuromuscul. Disord. 22, 368–379. https://doi.org/10.1016/j.nmd.2011.07.003.

11. Delfín, D.A., Zang, K.E., Schill, K.E., Patel, N.T., Janssen, P.M.L., Raman, S.V., and Rafael-Fortney, J.A. (2012). Cardiomyopathy in the dystrophin/utrophin-deficient mouse model of severe muscular dystrophy is characterized by dysregulation of matrix metalloproteinases. Neuromuscul. Disord. 22, 1006–1014. https://doi.org/10.1016/j.nmd.2012.05.002.

12. McGreevy, J.W., Hakim, C.H., McIntosh, M.A., and Duan, D. (2015). Animal models of Duchenne muscular dystrophy: from basic mechanisms to gene therapy. Dis. Model. Mech. 8, 195–213. https://doi.org/10.1242/dmm.018424.

13. Luo, M., and Anderson, M.E. (2013). Mechanisms of altered Ca(2)(+) handling in heart failure. Circ. Res. 113, 690–708. https://doi.org/10.1161/CIRCRESAHA.113.301651.

14. Zima, A.V., Bovo, E., Mazurek, S.R., Rochira, J.A., Li, W., and Terentyev, D. (2014). Ca handling during excitation-contraction coupling in heart failure. Pflügers Archiv 466, 1129–1137. https://doi.org/10.1007/s00424-014-1469-3.

15. Yuan, Q., Fan, G.C., Dong, M., Altschafl, B., Diwan, A., Ren, X., Hahn, H.H., Zhao, W., Waggoner, J.R., Jones, L.R., et al. (2007). Sarcoplasmic reticulum calcium overloading in junctin deficiency enhances cardiac contractility but increases ventricular automaticity. Circulation 115, 300–309. https://doi.org/10.1161/CIRCULATIONAHA.106.654699.

16. Chopra, N., Kannankeril, P.J., Yang, T., Hlaing, T., Holinstat, I., Ettensohn, K., Pfeifer, K., Akin, B., Jones, L.R., Franzini-Armstrong, C., and Knollmann, B.C. (2007). Modest reductions of cardiac calsequestrin increase sarcoplasmic reticulum Ca2+ leak independent of luminal Ca2+ and trigger ventricular arrhythmias in mice. Circ. Res. 101, 617–626. https://doi.org/10.1161/CIRCRESAHA.107.157552.

17. Rohman, M.S., Emoto, N., Takeshima, Y., Yokoyama, M., and Matsuo, M. (2003). Decreased mAKAP, ryanodine receptor, and SERCA2a gene expression in mdx hearts. Biochem. Biophys. Res. Commun. 310, 228–235. https://doi.org/10.1016/j.bbrc.2003.09.005.

18. Shin, J.H., Bostick, B., Yue, Y., Hajjar, R., and Duan, D. (2011). SERCA2a gene transfer improves electrocardiographic performance in aged mdx mice. J. Transl. Med. 9, 132. https://doi.org/10.1186/1479-5876-9-132.

19. He, L., and Hannon, G.J. (2004). MicroRNAs: small RNAs with a big role in gene regulation. Nat. Rev. Genet. 5, 522–531. https://doi.org/10.1038/nrg1379.

20. Wahlquist, C., Jeong, D., Rojas-Muñoz, A., Kho, C., Lee, A., Mitsuyama, S., van Mil, A., Park, W.J., Sluijter, J.P.G., Doevendans, P.A.F., et al. (2014). Inhibition of miR-25 improves cardiac contractility in the failing heart. Nature 508, 531–535. https://doi.org/10.1038/nature13073.

21. Nelson, C.A., Hunter, R.B., Quigley, L.A., Girgenrath, S., Weber, W.D., McCullough, J.A., Dinardo, C.J., Keefe, K.A., Ceci, L., Clayton, N.P., et al. (2011). Inhibiting TGF-beta activity improves respiratory function in mdx mice. Am. J. Pathol. 178, 2611–2621. https://doi.org/10.1016/j.ajpath.2011.02.024.

22. Wang, B., Hao, J., Jones, S.C., Yee, M.S., Roth, J.C., and Dixon, I.M.C. (2002). Decreased Smad 7 expression contributes to cardiac fibrosis in the infarcted rat heart. Am. J. Physiol. Heart Circ. Physiol. 282, H1685–H1696. https://doi.org/10.1152/ajpheart.00266.2001.

23. Yan, X., Liu, Z., and Chen, Y. (2009). Regulation of TGF-beta signaling by Smad7. Acta Biochim. Biophys. Sin. 41, 263–272. https://doi.org/10.1093/abbs/gmp018.

24. Huebner, K.D., Jassal, D.S., Halevy, O., Pines, M., and Anderson, J.E. (2008). Functional resolution of fibrosis in mdx mouse dystrophic heart and skeletal muscle by halofuginone. Am. J. Physiol. Heart Circ. Physiol. 294, H1550–H1561. https://doi.org/10.1152/ajpheart.01253.2007.

25. Ieronimakis, N., Hays, A.L., Janebodin, K., Mahoney, W.M., Jr., Duffield, J.S., Majesky, M.W., and Reyes, M. (2013). Coronary adventitial cells are linked to perivascular cardiac fibrosis via TGFbeta1 signaling in the mdx mouse model of Duchenne muscular dystrophy. J. Mol. Cell. Cardiol. 63, 122–134. https://doi.org/10.1016/j.yjmcc.2013.07.014.

26. Li, F., Liu, J., and Li, S. (2013). MicorRNA 106b approximately 25 cluster and gastric cancer. Surg. Oncol. 22, e7–e10. https://doi.org/10.1016/j.suronc.2013.01.003.

27. Li, Q., Zou, C., Zou, C., Han, Z., Xiao, H., Wei, H., Wang, W., Zhang, L., Zhang, X., Tang, Q., et al. (2013). MicroRNA-25 functions as a potential tumor suppressor in colon cancer by targeting Smad7. Cancer Lett. 335, 168–174. https://doi.org/10.1016/j.canlet.2013.02.029.

28. Smith, A.L., Iwanaga, R., Drasin, D.J., Micalizzi, D.S., Vartuli, R.L., Tan, A.C., and Ford, H.L. (2012). The miR-106b-25 cluster targets Smad7, activates TGF-beta signaling, and induces EMT and tumor initiating cell characteristics downstream of Six1 in human breast cancer. Oncogene 31, 5162–5171. https://doi.org/10.1038/onc.2012.11.

29. Haraguchi, T., Ozaki, Y., and Iba, H. (2009). Vectors expressing efficient RNA decoys achieve the long-term suppression of specific microRNA activity in mammalian cells. Nucleic Acids Res. 37, e43. https://doi.org/10.1093/nar/gkp040.

30. Bak, R.O., Hollensen, A.K., Primo, M.N., Sørensen, C.D., and Mikkelsen, J.G. (2013). Potent microRNA suppression by RNA Pol II-transcribed 'Tough Decoy' inhibitors. RNA 19, 280–293. https://doi.org/10.1261/rna.034850.112.

31. Xie, J., Ameres, S.L., Friedline, R., Hung, J.H., Zhang, Y., Xie, Q., Zhong, L., Su, Q., He, R., Li, M., et al. (2012). Long-term, efficient inhibition of microRNA function in mice using rAAV vectors. Nat. Methods 9, 403–409. https://doi.org/10.1038/nmeth.1903.

32. Bish, L.T., Morine, K., Sleeper, M.M., Sanmiguel, J., Wu, D., Gao, G., Wilson, J.M., and Sweeney, H.L. (2008). Adeno-associated virus (AAV) serotype 9 provides global cardiac gene transfer superior to AAV1, AAV6, AAV7, and AAV8 in the mouse and rat. Hum. Gene Ther. 19, 1359–1368. https://doi.org/10.1089/hum.2008.123.

33. Pacak, C.A., Mah, C.S., Thattaliyath, B.D., Conlon, T.J., Lewis, M.A., Cloutier, D.E., Zolotukhin, I., Tarantal, A.F., and Byrne, B.J. (2006). Recombinant adeno-associated virus serotype 9 leads to preferential cardiac transduction in vivo. Circ. Res. 99, e3–e9. https://doi.org/10.1161/01.RES.0000237661.18885.f6.

34. Cohen, T.V., Kollias, H.D., Liu, N., Ward, C.W., and Wagner, K.R. (2015). Genetic disruption of Smad7 impairs skeletal muscle growth and regeneration. J. Physiol. 593, 2479–2497. https://doi.org/10.1113/JP270201.

35. Zhou, L., Rafael-Fortney, J.A., Huang, P., Zhao, X.S., Cheng, G., Zhou, X., Kaminski, H.J., Liu, L., and Ransohoff, R.M. (2008). Haploinsufficiency of utrophin gene worsens skeletal muscle inflammation and fibrosis in mdx mice. J. Neurol. Sci. 264, 106–111. https://doi.org/10.1016/j.jns.2007.08.029.

36. Gutpell, K.M., Hrinivich, W.T., and Hoffman, L.M. (2015). Skeletal muscle fibrosis in the mdx/utrn+/- mouse validates its suitability as a murine model of Duchenne muscular dystrophy. PLoS One 10, e0117306. https://doi.org/10.1371/journal.pone.0117306.

37. Grady, R.M., Teng, H., Nichol, M.C., Cunningham, J.C., Wilkinson, R.S., and Sanes, J.R. (1997). Skeletal and cardiac myopathies in mice lacking utrophin and dystrophin: a model for Duchenne muscular dystrophy. Cell 90, 729–738. https://doi.org/10.1016/s0092-8674(00)80533-4.

38. Divakaran, V., Adrogue, J., Ishiyama, M., Entman, M.L., Haudek, S., Sivasubramanian, N., and Mann, D.L. (2009). Adaptive and maladptive effects of SMAD3 signaling in the adult heart after hemodynamic pressure overloading. Circ. Heart Fail. 2, 633–642. https://doi.org/10.1161/CIRCHEARTFAILURE.108.823070.

39. Li, J.H., Zhu, H.J., Huang, X.R., Lai, K.N., Johnson, R.J., and Lan, H.Y. (2002). Smad7 inhibits fibrotic effect of TGF-Beta on renal tubular epithelial cells by blocking Smad2 activation. J. Am. Soc. Nephrol. 13, 1464–1472. https://doi.org/10.1097/01.asn.0000014252.37680.e4.

40. Humeres, C., Shinde, A.V., Hanna, A., Alex, L., Hernández, S.C., Li, R., Chen, B., Conway, S.J., and Frangogiannis, N.G. (2022). Smad7 effects on TGF-beta and ErbB2 restrain myofibroblast activation and protect from postinfarction heart failure. J. Clin. Invest. 132, e146926. https://doi.org/10.1172/JCI146926.

41. Chung, A.C.K., Dong, Y., Yang, W., Zhong, X., Li, R., and Lan, H.Y. (2013). Smad7 suppresses renal fibrosis via altering expression of TGF-beta/Smad3-regulated microRNAs. Mol. Ther. 21, 388–398. https://doi.org/10.1038/mt.2012.251.

42. Coker, R.K., Laurent, G.J., Jeffery, P.K., du Bois, R.M., Black, C.M., and McAnulty, R.J. (2001). Localisation of transforming growth factor beta1 and beta3 mRNA transcripts in normal and fibrotic human lung. Thorax 56, 549–556. https://doi.org/10.1136/thorax.56.7.549.

43. Duan, D., Goemans, N., Takeda, S., Mercuri, E., and Aartsma-Rus, A. (2021). Duchenne muscular dystrophy. Nat. Rev. Dis. Prim. 7, 13. https://doi.org/10.1038/s41572-021-00248-3.

44. Rosenberg, A.S., Puig, M., Nagaraju, K., Hoffman, E.P., Villalta, S.A., Rao, V.A., Wakefield, L.M., and Woodcock, J. (2015). Immune-mediated pathology in Duchenne muscular dystrophy. Sci. Transl. Med. 7, 299rv4. https://doi.org/10.1126/scitranslmed.aaa7322.

45. Sugihara, H., Teramoto, N., Nakamura, K., Shiga, T., Shirakawa, T., Matsuo, M., Ogasawara, M., Nishino, I., Matsuwaki, T., Nishihara, M., and Yamanouchi, K.

(2020). Cellular senescence-mediated exacerbation of Duchenne muscular dystrophy. Sci. Rep. 10, 16385. https://doi.org/10.1038/s41598-020-73315-6.

46. Gilchrist, S.C., Ontell, M.P., Kochanek, S., and Clemens, P.R. (2002). Immune response to full-length dystrophin delivered to Dmd muscle by a high-capacity adenoviral vector. Mol. Ther. 6, 359–368. https://doi.org/10.1006/mthe.2002.0675.

47. Riaz, M., Raz, Y., Moloney, E.B., van Putten, M., Krom, Y.D., van der Maarel, S.M., Verhaagen, J., and Raz, V. (2015). Differential myofiber-type transduction preference of adeno-associated virus serotypes 6 and 9. Skeletal Muscle 5, 37. https://doi.org/10.1186/s13395-015-0064-4.

48. Chen, B.D., He, C.H., Chen, X.C., Pan, S., Liu, F., Ma, X., Li, X.M., Gai, M.T., Tao, J., Ma, Y.T., et al. (2015). Targeting transgene to the heart and liver with AAV9 by different promoters. Clin. Exp. Pharmacol. Physiol. 42, 1108–1117. https://doi.org/10.1111/1440-1681.12453.

49. Jin, Q., Qiao, C., Li, J., Li, J., and Xiao, X. (2018). Neonatal Systemic AAV-Mediated Gene Delivery of GDF11 Inhibits Skeletal Muscle Growth. Mol. Ther. 26, 1109–1117. https://doi.org/10.1016/j.ymthe.2018.01.016.

50. Kessler, P.D., Podsakoff, G.M., Chen, X., McQuiston, S.A., Colosi, P.C., Matelis, L.A., Kurtzman, G.J., and Byrne, B.J. (1996). Gene delivery to skeletal muscle results in sustained expression and systemic delivery of a therapeutic protein. Proc. Natl. Acad. Sci. USA 93, 14082–14087. https://doi.org/10.1073/pnas.93.24.14082.

51. Herzog, R.W., Hagstrom, J.N., Kung, S.H., Tai, S.J., Wilson, J.M., Fisher, K.J., and High, K.A. (1997). Stable gene transfer and expression of human blood coagulation factor IX after intramuscular injection of recombinant adeno-associated virus. Proc. Natl. Acad. Sci. USA 94, 5804–5809. https://doi.org/10.1073/pnas.94.11.5804.

52. Kay, M.A., Manno, C.S., Ragni, M.V., Larson, P.J., Couto, L.B., McClelland, A., Glader, B., Chew, A.J., Tai, S.J., Herzog, R.W., et al. (2000). Evidence for gene transfer and expression of factor IX in haemophilia B patients treated with an AAV vector. Nat. Genet. 24, 257–261. https://doi.org/10.1038/73464.

53. Song, S., Scott-Jorgensen, M., Wang, J., Poirier, A., Crawford, J., Campbell-Thompson, M., and Flotte, T.R. (2002). Intramuscular administration of recombinant adeno-associated virus 2 alpha-1 antitrypsin (rAAV-SERPINA1) vectors in a nonhuman primate model: safety and immunologic aspects. Mol. Ther. 6, 329–335. https://doi.org/10.1006/mthe.2002.0673.

54. Toromanoff, A., Chérel, Y., Guilbaud, M., Penaud-Budloo, M., Snyder, R.O., Haskins, M.E., Deschamps, J.Y., Guigand, L., Podevin, G., Arruda, V.R., et al. (2008). Safety and Efficacy of Regional Intravenous (RI) Versus Intramuscular (IM) Delivery of rAAV1 and rAAV8 to Nonhuman Primate Skeletal Muscle. Mol. Ther. 16, 1291–1299. https://doi.org/10.1038/mt.2008.87.

55. Bostick, B., Shin, J.H., Yue, Y., Wasala, N.B., Lai, Y., and Duan, D. (2012). AAV micro-dystrophin gene therapy alleviates stress-induced cardiac death but not myocardial fibrosis in >21-m-old mdx mice, an end-stage model of Duchenne muscular dystrophy cardiomyopathy. J. Mol. Cell. Cardiol. 53, 217–222. https://doi.org/10.1016/j.yjmcc.2012.05.002.

56. Jarmin, S., Kymalainen, H., Popplewell, L., and Dickson, G. (2014). New developments in the use of gene therapy to treat Duchenne muscular dystrophy. Expet Opin. Biol. Ther. 14, 209–230. https://doi.org/10.1517/14712598.2014.866087.

57. Jeong, D., Yoo, J., Lee, P., Kepreotis, S.V., Lee, A., Wahlquist, C., Brown, B.D., Kho, C., Mercola, M., and Hajjar, R.J. (2018). miR-25 Tough Decoy Enhances Cardiac Function in Heart Failure. Mol. Ther. 26, 718–729. https://doi.org/10.1016/j.ymthe.2017.11.014.

58. Wasala, N.B., Yue, Y., Lostal, W., Wasala, L.P., Niranjan, N., Hajjar, R.J., Babu, G.J., and Duan, D. (2020). Single SERCA2a Therapy Ameliorated Dilated Cardiomyopathy for 18 Months in a Mouse Model of Duchenne Muscular Dystrophy. Mol. Ther. 28, 845–854. https://doi.org/10.1016/j.ymthe.2019.12.011.

59. Morales, E.D., Yue, Y., Watkins, T.B., Han, J., Pan, X., Gibson, A.M., Hu, B., Brito-Estrada, O., Yao, G., Makarewich, C.A., et al. (2023). Dwarf Open Reading Frame (DWORF) Gene Therapy Ameliorated Duchenne Muscular Dystrophy Cardiomyopathy in Aged mdx Mice. J. Am. Heart Assoc. 12, e027480. https://doi.org/10.1161/JAHA.122.027480.

60. Law, M.L., Cohen, H., Martin, A.A., Angulski, A.B.B., and Metzger, J.M. (2020). Dysregulation of Calcium Handling in Duchenne Muscular Dystrophy-Associated Dilated Cardiomyopathy: Mechanisms and Experimental Therapeutic Strategies. J. Clin. Med. 9, 520. https://doi.org/10.3390/jcm9020520.

61. Nakamura, A., Yoshida, K., Ueda, H., Takeda, S., and Ikeda, S.i. (2005). Up-regulation of mitogen activated protein kinases in mdx skeletal muscle following chronic treadmill exercise. Biochim. Biophys. Acta 1740, 326–331. https://doi.org/10.1016/j.bbadis.2004.12.003.

62. Kolodziejczyk, S.M., Walsh, G.S., Balazsi, K., Seale, P., Sandoz, J., Hierlihy, A.M., Rudnicki, M.A., Chamberlain, J.S., Miller, F.D., and Megeney, L.A. (2001). Activation of JNK1 contributes to dystrophic muscle pathogenesis. Curr. Biol. 11, 1278–1282. https://doi.org/10.1016/s0960-9822(01)00397-9.

63. Wissing, E.R., Boyer, J.G., Kwong, J.Q., Sargent, M.A., Karch, J., McNally, E.M., Otsu, K., and Molkentin, J.D. (2014). P38alpha MAPK underlies muscular dystrophy and myofiber death through a Bax-dependent mechanism. Hum. Mol. Genet. 23, 5452–5463. https://doi.org/10.1093/hmg/ddu270.

64. Pillai-Kastoori, L., Schutz-Geschwender, A.R., and Harford, J.A. (2020). A systematic approach to quantitative Western blot analysis. Anal. Biochem. 593, 113608. https://doi.org/10.1016/j.ab.2020.113608.

65. Assaf, B.T., and Whiteley, L.O. (2018). Considerations for Preclinical Safety Assessment of Adeno-Associated Virus Gene Therapy Products. Toxicol. Pathol. 46, 1020–1027. https://doi.org/10.1177/0192623318803867.

66. Tong, J.G., Evans, A.C., Ho, M.L., Guenther, C.M., Brun, M.J., Judd, J., Wu, E., and Suh, J. (2019). Reducing off target viral delivery in ovarian cancer gene therapy using a protease-activated AAV2 vector platform. J. Control Release. 307, 292–301. https://doi.org/10.1016/j.jconrel.2019.06.034.

67. Pacak, C.A., Sakai, Y., Thattaliyath, B.D., Mah, C.S., and Byrne, B.J. (2008). Tissue specific promoters improve specificity of AAV9 mediated transgene expression following intra-vascular gene delivery in neonatal mice. Genet. Vaccine Ther. 6, 13. https://doi.org/10.1186/1479-0556-6-13.

68. Au, H.K.E., Isalan, M., and Mielcarek, M. (2021). Gene Therapy Advances: A Meta-Analysis of AAV Usage in Clinical Settings. Front. Med. 8, 809118. https://doi.org/10.3389/fmed.2021.809118.

69. Rodriguez-Estevez, L., Asokan, P., and Borrás, T. (2020). Transduction optimization of AAV vectors for human gene therapy of glaucoma and their reversed cell entry characteristics. Gene Ther. 27, 127–142. https://doi.org/10.1038/s41434-019-0105-4.

70. Colón-Thillet, R., Jerome, K.R., and Stone, D. (2021). Optimization of AAV vectors to target persistent viral reservoirs. Virol. J. 18, 85. https://doi.org/10.1186/s12985-021-01555-7.

71. Harada, M., Luo, X., Murohara, T., Yang, B., Dobrev, D., and Nattel, S. (2014). MicroRNA regulation and cardiac calcium signaling: role in cardiac disease and therapeutic potential. Circ. Res. 114, 689–705. https://doi.org/10.1161/CIRCRESAHA.114.301798.

72. Dangwal, S., and Thum, T. (2014). microRNA therapeutics in cardiovascular disease models. Annu. Rev. Pharmacol. Toxicol. 54, 185–203. https://doi.org/10.1146/annurev-pharmtox-011613-135957.

73. Maegdefessel, L. (2014). The emerging role of microRNAs in cardiovascular disease. J. Intern. Med. 276, 633–644. https://doi.org/10.1111/joim.12298.

74. Olson, E.N. (2014). MicroRNAs as therapeutic targets and biomarkers of cardiovascular disease. Sci. Transl. Med. 6, 239ps3. https://doi.org/10.1126/scitranslmed.3009008.

75. Small, E.M., and Olson, E.N. (2011). Pervasive roles of microRNAs in cardiovascular biology. Nature 469, 336–342. https://doi.org/10.1038/nature09783.

76. Pacher, P., Nagayama, T., Mukhopadhyay, P., Bátkai, S., and Kass, D.A. (2008). Measurement of cardiac function using pressure-volume conductance catheter technique in mice and rats. Nat. Protoc. 3, 1422–1434. https://doi.org/10.1038/nprot.2008.138.

77. Oh, J.G., Jeong, D., Cha, H., Kim, J.M., Lifirsu, E., Kim, J., Yang, D.K., Park, C.S., Kho, C., Park, S., et al. (2012). PICOT increases cardiac contractility by inhibiting PKCzeta activity. J. Mol. Cell. Cardiol. 53, 53–63. https://doi.org/10.1016/j.yjmcc.2012.03.005.

78. Li, S., Zhuang, C., Niu, C.M., Bao, Y., Xie, Q., and Lan, N. (2017). Evaluation of Functional Correlation of Task-Specific Muscle Synergies with Motor Performance in Patients Poststroke. Front. Neurol. 8, 337. https://doi.org/10.3389/fneur.2017.00337.